J. Fluid Mech. (2000), *vol.* 410, *pp.* 147–183. Printed in the United Kingdom

Three-dimensional wave distortion and disintegration of thin planar liquid sheets

By INCHUL KIM† AND WILLIAM A. SIRIGNANO

Department of Mechanical and Aerospace Engineering, University of California, Irvine, CA 92697, USA

(Received 26 June 1999 and in revised form 23 November 1999)

Three-dimensional dilational and sinuous wave propagation on infinite or semi-infinite thin planar sheets flowing into a gas of negligible density is investigated. The assumption of thin sheets allows the reduction of the problem dimensionality by integration across the sheet thickness. For finite-amplitude disturbances, the strongest nonlinear effects occur when the cross-sectional wavenumber (l) is close to the streamwise wavenumber (k). First, dilational wave propagation is considered. When l is close to k for infinite sheets, higher harmonics are generated in the streamwise direction, and the standing wave with finite amplitude in the cross-sectional plane becomes flat. As time passes, the waves return to the initial wave shape. This process is repeated in a cycle. A similar phenomenon is found in semi-infinite sheets with low Weber number. When l is close to k for semi-infinite sheets and Weber number is high, fluid accumulates into fluid lumps interspaced by one wavelength in the cross-sectional direction as well as in the streamwise direction. This leads to the formation of initially non-spherical ligaments or large droplets from the liquid sheet. Secondly, sinuous wave propagation is considered. When l is close to k for semi-infinite sheets and Weber number is high, fluid agglomerates in the edge of the sheet interspaced by half a wavelength in the cross-sectional direction as well as in the streamwise direction. A three-dimensional visualization of the computational results shows that the disturbance at the nozzle exit induces fluid to agglomerate into half-spherical lumps, which indicate the formation of ligaments or large droplets from the liquid sheet. A similar phenomenon is found in the case of infinite sheets.

1. Introduction

Atomization is an important process in many applications such as spray combustion and sprayers for agricultural or domestic usage. Also, atomization should be avoided in other applications, e.g. curtain coating. Many atomization systems rely on large liquid surface-to-volume ratio to increase the rate of disintegration. Thin sheets of injected liquid are a very common mechanism for optimizing interface area.

The mechanism of liquid sheet instability and breakup has been investigated experimentally and theoretically by numerous authors. Hagerty & Shea (1955) found that only two types of waves are possible on a flat liquid sheet at any given frequency. The first type is the antisymmetric (sinuous) mode where the two sheet surfaces are in phase according to linear theory; the other type is the symmetric (dilational) mode where linear theory predicts that the two sheet surfaces are out of phase. The sinuous mode is more unstable than the dilational mode when the gas-to-liquid density ratio

† Present address: Department of Mechanical Engineering, The University of Michigan – Dearborn, MI 48128, USA.

is low (Dombrowski & Hooper 1962; Li & Tankin 1991; Mansour & Chigier 1991); conversely, the dilational mode is more unstable than the sinuous mode when the density ratio is high (Rangel & Sirignano 1991).

Many theoretical investigations were based on linear temporal analyses on an infinitely long liquid sheet. For thin sheets, Taylor (1959*a*), Lin & Roberts (1981), and Mehring & Sirignano (1999) observed that linear dilational waves are dispersive; conversely, linear sinuous waves are non-dispersive. These linear temporal analyses predict that an optimal frequency exists where the growth rate is a maximum when the gas-phase density is included in the analyses. However, Crapper, Dombrowski & Pyott (1975) and Crapper & Dombrowski (1984) suggested and found experimentally that dominant waves observed on a liquid sheet must be of a frequency imposed by some external source. This finding suggests that investigations of liquid sheets modulated at the nozzle exit are more important in practical applications than those of liquid sheets with infinite length. However, rather few studies of the former have been done. In the case of round jets, Bogy (1978) performed linear analysis of wave propagation and instability (symmetric mode) in a round liquid jet of semi-infinite length harmonically forced at the nozzle exit and issuing into a void. Later, for the sheet case, Mehring & Sirignano (1999) performed linear analyses and nonlinear numerical analyses of wave distortion and disintegration in two-dimensional planar liquid sheets of semi-infinite length modulated at the nozzle exit and issuing in a void. Also, liquid sheets issuing from air-blast atomizers can be treated as liquid sheets modulated at the nozzle exit. From their experiments on the aerodynamic instability of liquid sheets issuing from a two-dimensional air-assisted nozzle, Mansour & Chigier (1990, 1991) showed that the effect of introducing air in the nozzle is similar to the effect of forced vibrations at the nozzle exit.

Through linear analyses (of modulated or unmodulated sheets), one can find a dispersion relationship between wavenumber and frequency for both the dilational and sinuous modes. However, linear analyses do not predict sheet breakup due to the sinuous mode. The reason is that the sinuous mode is decoupled from the dilational mode when the governing equations are linearized (see § 4 in the present paper; Squire 1953; Taylor 1959*b*), and sheet breakup cannot occur without variation of the sheet thickness.

A few nonlinear analyses have been reported. Clark & Dombrowski (1972) studied the aerodynamic growth of sinuous waves on parallel-sided inviscid liquid sheets through a second-order analysis and equations that describe the characteristics or the fundamental mode and the first harmonic. They found that thinning of the sheet is caused by the growth of the harmonic wave, and maximum thinning and subsequent rupture occur at positions corresponding to 3/8 and 7/8 of the wavelength of the fundamental wave. In other words, the sheet breaks up at half wavelengths of the fundamental wave. Asare, Takhashi & Hoffman (1981) performed experiments on planar sheet water issuing vertically downward from slit nozzles which were subjected to transverse forced harmonic excitation. They found that, for large-amplitude nozzle excitation, the waveform becomes highly nonlinear and non-sinusoidal and can resemble a sawtooth waveform in some cases. Rangel & Sirignano (1991) performed a linear analysis and a nonlinear analysis using a vortex discretization method and considered two-dimensional temporal dilational and sinuous instability of a sheet of finite thickness including the complete range of density ratio (gas to liquid) and thickness-to-wavelength ratio. They found that sinuous modes may result in ligaments interspaced by half a wavelength and dilational modes may result in ligaments interspaced by one wavelength. Mehring & Sirignano (1999) analysed linear and

nonlinear dilational and sinuous waves on thin inviscid infinite and semi-infinite planar liquid sheets in a gas of negligible density by means of a method that reduces the two-dimensional unsteady problem to a one-dimensional unsteady problem. They found the same type of sheet breakup as Rangel & Sirignano (1991) did and a sawtooth wave shape for the nonlinear sinuous mode as Asare *et al.* (1981) observed experimentally.

All the nonlinear analyses mentioned above are restricted to two-dimensionality. Practically, the breakup of a liquid sheet into the major ligaments and droplets can be predicted only with a three-dimensional nonlinear representation. The objective of the present paper is to examine three-dimensional effects on thin inviscid infinite planar liquid sheets and modulated semi-infinite planar liquid sheets in a gas of negligible density by means of a similar approach to that of Mehring & Sirignano (1999) who reduced the two-dimensional unsteady problem to a one-dimensional unsteady problem. In the following sections, results from three-dimensional computations are compared with those from two-dimensional computations by Mehring & Sirignano (1999). All the results for the cross-sectional wavenumber (l) equal to zero in this paper correspond to those from two-dimensional computations.

As mentioned above, the gas density is neglected in the present paper. Rangel & Sirignano (1991) showed that the Kelvin–Helmholtz instability is small compared to the capillary force when the density ratio of gas to liquid is small as in the case that water is injected into the air under normal atmospheric pressure. For example, the density ratio of the air to water is 0.001.

The next section provides a mathematical description of the flow considered, the governing equations, and the numerical solution procedure. In § 3, linear and nonlinear analyses are performed for the dilational mode (§ 3.1 and § 3.2) and the sinuous mode (§ 3.3 and § 3.4) on infinitely long liquid sheets. In § 4, linear and nonlinear analyses are performed for the dilational mode (§ 4.1 and § 4.2) and the sinuous mode (§ 4.3 and § 4.4) on semi-infinitely long liquid sheets which are harmonically forced at the nozzle exit. Section 5 provides a summary of the work.

2. Formulation and governing equations

A thin liquid sheet infinitely or semi-infinitely long in the flow direction (x) is considered as shown in figure 1. The liquid sheet is initially injected into a gas of negligible density compared to the liquid density with the undisturbed velocity u_o and the undisturbed thickness a_o. The liquid is assumed inviscid, incompressible, and free of gravity force. Then, the continuity and momentum equations governing the liquid motion are

$$\frac{\partial u}{\partial x} + \frac{\partial v}{\partial y} + \frac{\partial w}{\partial z} = 0, \tag{1}$$

$$\frac{\partial u}{\partial t} + \frac{\partial u^2}{\partial x} + \frac{\partial uv}{\partial y} + \frac{\partial uw}{\partial z} + \frac{1}{\rho}\frac{\partial p}{\partial x} = 0, \tag{2}$$

$$\frac{\partial w}{\partial t} + \frac{\partial uw}{\partial x} + \frac{\partial vw}{\partial y} + \frac{\partial w^2}{\partial z} + \frac{1}{\rho}\frac{\partial p}{\partial z} = 0, \tag{3}$$

$$\frac{\partial v}{\partial t} + \frac{\partial uv}{\partial x} + \frac{\partial v^2}{\partial y} + \frac{\partial vw}{\partial z} + \frac{1}{\rho}\frac{\partial p}{\partial y} = 0. \tag{4}$$

The upper boundary of the liquid sheet is given by $y_+(x, z, t)$ while the lower boundary is described as $y_-(x, z, t)$. A surface tension σ exists at the boundaries and affects

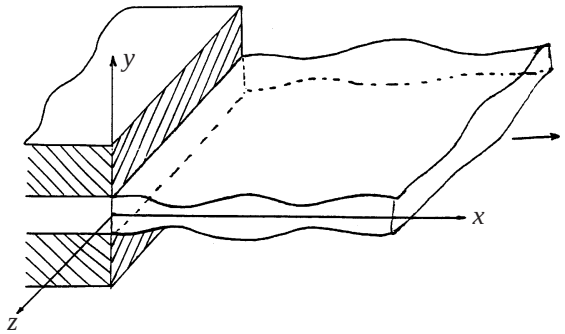

FIGURE 1. Flow geometry and coordinates.

the force balance at the interfaces. The boundary conditions at the upper and lower surfaces are

$$v_{\pm} = \frac{\partial y_{\pm}}{\partial t} + u_{\pm}\frac{\partial y_{\pm}}{\partial x} + w_{\pm}\frac{\partial y_{\pm}}{\partial z}, \tag{5}$$

$$p_{\pm} = \sigma\left(\frac{1}{R_{1\pm}} + \frac{1}{R_{2\pm}}\right) = \frac{\pm\sigma}{(1+y_x^2+y_z^2)_{\pm}^{3/2}}[y_{xx}(1+y_z^2) + y_{zz}(1+y_x^2) - 2y_x y_z y_{xz}]_{\pm}, \tag{6}$$

where the subscripts + and − denote values at the upper and lower sheet surfaces, respectively, and $R_{1\pm}$ and $R_{2\pm}$ are the principal radii of curvature of the surface. The subscripts x and z denote derivatives with respect to x and z, respectively. Equations (5) and (6) are called kinematic and dynamic boundary conditions, respectively.

Define the sheet thickness, $\tilde{y}(x,z,t)$, and the displacement of the sheet, $\bar{y}(x,z,t)$, to be

$$\tilde{y}(x,z,t) = y_+ - y_-, \qquad \bar{y}(x,z,t) = (y_+ + y_-)/2. \tag{7}$$

Also define Δp and $\bar{p}$ in a similar fashion. They are related to $\tilde{y}$ and $\bar{y}$ by using (6) and (7) to yield

$$\begin{aligned}\Delta p = p_+ - p_- = -\sigma\Big[&(f_{1+}+f_{1-})\frac{\partial^2\bar{y}}{\partial x^2} + \tfrac{1}{2}(f_{1+}-f_{1-})\frac{\partial^2\tilde{y}}{\partial x^2} + (f_{2+}+f_{2-})\frac{\partial^2\bar{y}}{\partial z^2}\\ &+\tfrac{1}{2}(f_{2+}-f_{2-})\frac{\partial^2\tilde{y}}{\partial z^2} + (f_{3+}+f_{3-})\frac{\partial^2\bar{y}}{\partial x\partial z} + \tfrac{1}{2}(f_{3+}-f_{3-})\frac{\partial^2\tilde{y}}{\partial x\partial z}\Big],\end{aligned} \tag{8}$$

$$\begin{aligned}\bar{p} = (p_+ + p_-)/2 = -\frac{\sigma}{2}\Big[&(f_{1+}-f_{1-})\frac{\partial^2\bar{y}}{\partial x^2} + \tfrac{1}{2}(f_{1+}+f_{1-})\frac{\partial^2\tilde{y}}{\partial x^2} + (f_{2+}-f_{2-})\frac{\partial^2\bar{y}}{\partial z^2}\\ &+\tfrac{1}{2}(f_{2+}+f_{2-})\frac{\partial^2\tilde{y}}{\partial z^2} + (f_{3+}-f_{3-})\frac{\partial^2\bar{y}}{\partial x\partial z} + \tfrac{1}{2}(f_{3+}+f_{3-})\frac{\partial^2\tilde{y}}{\partial x\partial z}\Big],\end{aligned} \tag{9}$$

where f_{1+}, f_{1-}, f_{2+}, f_{2-}, f_{3+}, and f_{3-} are defined as

$$f_{1\pm} = \frac{1+(\bar{y}_z \pm \frac{1}{2}\tilde{y}_z)^2}{[1+(\bar{y}_x \pm \frac{1}{2}\tilde{y}_x)^2 + (\bar{y}_z \pm \frac{1}{2}\tilde{y}_z)^2]^{3/2}}, \tag{10a}$$

$$f_{2\pm} = \frac{1+(\bar{y}_x \pm \frac{1}{2}\tilde{y}_x)^2}{[1+(\bar{y}_x \pm \frac{1}{2}\tilde{y}_x)^2 + (\bar{y}_z \pm \frac{1}{2}\tilde{y}_z)^2]^{3/2}}, \tag{10b}$$

$$f_{3\pm} = \frac{-2(\bar{y}_x \pm \frac{1}{2}\tilde{y}_x)(\bar{y}_z \pm \frac{1}{2}\tilde{y}_z)}{[1+(\bar{y}_x \pm \frac{1}{2}\tilde{y}_x)^2 + (\bar{y}_z \pm \frac{1}{2}\tilde{y}_z)^2]^{3/2}}. \tag{10c}$$

We also define $\Delta\phi$ and $\bar{\phi}$ for later use as

$$\Delta\phi = 2\Delta p/\sigma, \qquad \bar{\phi} = 2\bar{p}/\sigma. \tag{11}$$

For a sheet whose thickness is small compared to the wavelength of a disturbance, we can consider u, $\partial v/\partial y$, w and $\partial p/\partial y$ to be nearly constant with variation of y. For the two-dimensional disturbance, Mehring & Sirignano (1999) showed that these behaviours were predicted as the leading behaviour in an asymptotic representation for long wavelengths. The problem can therefore be reduced to a two-dimensional, unsteady formulation. We define average velocities $\bar{u}(x,z,t)$, $\bar{v}(x,z,t)$, and $\bar{w}(x,z,t)$ to be

$$\bar{u}(x,z,t) = \frac{1}{\tilde{y}}\int_{y_-}^{y_+} u\,\mathrm{d}y, \quad \bar{v}(x,z,t) = \frac{1}{\tilde{y}}\int_{y_-}^{y_+} v\,\mathrm{d}y, \quad \bar{w}(x,z,t) = \frac{1}{\tilde{y}}\int_{y_-}^{y_+} w\,\mathrm{d}y. \tag{12}$$

Average pressure $\bar{p}(x,z,t)$ is defined in a similar manner. Equations (1)–(4) can be integrated term-by-term from y_- to y_+ and incorporated into the kinematic and dynamic boundary conditions ((5) and (6)) and the above definitions. The results are

$$\frac{\partial\tilde{y}}{\partial t} + \frac{\partial\tilde{y}\bar{u}}{\partial x} + \frac{\partial\tilde{y}\bar{w}}{\partial z} = 0, \tag{13}$$

$$\frac{\partial\bar{u}}{\partial t} + \bar{u}\frac{\partial\bar{u}}{\partial x} + \bar{w}\frac{\partial\bar{u}}{\partial z} = -\frac{1}{\rho}\left(\frac{\partial\bar{p}}{\partial x} - \frac{\Delta p}{\tilde{y}}\frac{\partial\bar{y}}{\partial x}\right), \tag{14}$$

$$\frac{\partial\bar{w}}{\partial t} + \bar{u}\frac{\partial\bar{w}}{\partial x} + \bar{w}\frac{\partial\bar{w}}{\partial z} = -\frac{1}{\rho}\left(\frac{\partial\bar{p}}{\partial z} - \frac{\Delta p}{\tilde{y}}\frac{\partial\bar{y}}{\partial z}\right), \tag{15}$$

$$\frac{\partial\bar{v}}{\partial t} + \bar{u}\frac{\partial\bar{v}}{\partial x} + \bar{w}\frac{\partial\bar{v}}{\partial z} = -\frac{1}{\rho}\frac{\Delta p}{\tilde{y}}. \tag{16}$$

Equations (13)–(16) show that the number of unknowns is five ($\bar{y}$, $\tilde{y}$, u, v, and w) but the number of equations is four. An additional equation is obtained by combining the kinematic boundary conditions for v_+ and v_-, and by using $\bar{v} = (v_+ + v_-)/2$. Mehring & Sirignano (1999) showed that v can be expressed by a polynomial expansion in terms of y or $(y - \bar{y})$. As a consequence, v can be expressed as a linear function of y by the first-order approximation. Thus, the expression $\bar{v} = (v_+ + v_-)/2$ is consistent with (12) by the first-order approximation:

$$\bar{v} = \frac{\partial\bar{y}}{\partial t} + \bar{u}\frac{\partial\bar{y}}{\partial x} + \bar{w}\frac{\partial\bar{y}}{\partial z}. \tag{17}$$

For two-dimensional planar sheet distortion, (13)–(17) agree with the results of Mehring & Sirignano (1999).

The system of equations (13) to (17) is solved by finite-difference computations. The finite-difference technique employed in this paper is the Richtmyer splitting of the Lax–Wendroff method (Ferziger 1981). For example, (14) can be re-written as

$$\frac{\partial\bar{u}}{\partial t} + \bar{u}\frac{\partial\bar{u}}{\partial x} + \bar{w}\frac{\partial\bar{u}}{\partial z} = f(t,x,z).$$

The discretization of this equation involves two steps as follows:

$$\frac{u_{j,k}^{n+1/2} - (u_{j+1,k}^{n} + u_{j-1,k}^{n} + u_{j,k+1}^{n} + u_{j,k-1}^{n})/4}{\Delta t/2} + u_{j,k}^{n}\frac{u_{j+1,k}^{n} - u_{j-1,k}^{n}}{2\Delta x} + w_{j,k}^{n}\frac{u_{j,k+1}^{n} - u_{j,k-1}^{n}}{2\Delta z} = f_{j,k}^{n},$$

$$\frac{u_{j,k}^{n+1} - u_{j,k}^{n}}{\Delta t} + u_{j,k}^{n+1/2}\frac{(u_{j+1,k} - u_{j-1,k})^{n+1/2}}{2\Delta x} + w_{j,k}^{n+1/2}\frac{(u_{j,k+1} - u_{j,k-1})^{n+1/2}}{2\Delta z} = f_{j,k}^{n+1/2},$$

where the spatial derivatives with respect to x or z in $f(t,x,z)$ as indicated by (8)–(10) are discretized with the second-order central-difference scheme. This Richtmyer's method can be regarded as a predictor-corrector method with a first-order Lax predictor and a second-order leapfrog corrector (Ferziger 1981).

The magnitudes of mesh size and time step employed in the computation are given in each section. Accuracy of the numerical solutions has been examined by successive refinement of mesh size and time step.

3. Liquid sheet with infinite length

For the motion of infinitely long thin liquid sheets, we introduce the Galilean transformation in the x-direction as

$$X = x - u_o t, \quad Y = y, \quad Z = z, \quad \tau = t, \tag{18}$$

and define $\bar{u}_1 \equiv \bar{u} - u_o$. Furthermore, all the variables are normalized using the undisturbed sheet thickness a_o as the characteristic length and $\sqrt{\sigma/(2\rho a_o)}$ as the characteristic velocity. Taylor (1959*a*) derived that the wave speeds of the dilational mode and the sinuous mode of infinitely long (not necessarily thin) liquid sheets are proportional to $\sqrt{\sigma/(2\rho a_o)}$. Then equations (13)–(16) are transformed to

$$\frac{\partial \tilde{y}^*}{\partial \tau^*} + \frac{\partial \tilde{y}^* \bar{u}_1^*}{\partial X^*} + \frac{\partial \tilde{y}^* \bar{w}^*}{\partial Z^*} = 0, \tag{19}$$

$$\frac{\partial \bar{u}_1^*}{\partial \tau^*} + \bar{u}_1^* \frac{\partial \bar{u}_1^*}{\partial X^*} + \bar{w}^* \frac{\partial \bar{u}_1^*}{\partial Z^*} = -\left(\frac{\partial \bar{\phi}^*}{\partial X^*} - \frac{\Delta \phi^*}{\tilde{y}^*} \frac{\partial \bar{y}^*}{\partial X^*} \right), \tag{20}$$

$$\frac{\partial \bar{w}^*}{\partial \tau^*} + \bar{u}_1^* \frac{\partial \bar{w}^*}{\partial X^*} + \bar{w}^* \frac{\partial \bar{w}^*}{\partial Z^*} = -\left(\frac{\partial \bar{\phi}^*}{\partial Z^*} - \frac{\Delta \phi^*}{\tilde{y}^*} \frac{\partial \bar{y}^*}{\partial Z^*} \right), \tag{21}$$

$$\frac{\partial \bar{v}^*}{\partial \tau^*} + \bar{u}_1^* \frac{\partial \bar{v}^*}{\partial X^*} + \bar{w}^* \frac{\partial \bar{v}^*}{\partial Z^*} = -\frac{\Delta \phi^*}{\tilde{y}^*}, \tag{22}$$

$$\bar{v}^* = \frac{\partial \bar{y}^*}{\partial \tau^*} + \bar{u}_1^* \frac{\partial \bar{y}^*}{\partial X^*} + \bar{w}^* \frac{\partial \bar{y}^*}{\partial Z^*}, \tag{23}$$

where $*$ denotes the dimensionless quantity and will be dropped in the rest of the paper.

Equations (19)–(23) can be linearized as follows. Let $\tilde{y} = 1 + \tilde{y}'$, $\bar{y} = \bar{y}'$, $\bar{u}_1 = \bar{u}'$, $\bar{v} = \bar{v}'$, and $\bar{w} = \bar{w}'$. Insert these into (19)–(23) and assume that the primed quantities are small. After neglecting the higher-order terms, we get

$$\frac{\partial \tilde{y}'}{\partial \tau} + \frac{\partial}{\partial X}(\tilde{y}' + \bar{u}') + \frac{\partial \bar{w}'}{\partial Z} = 0, \tag{24}$$

$$\frac{\partial \bar{u}'}{\partial \tau} + \frac{\partial \bar{u}'}{\partial X} = \frac{\partial}{\partial X} \left(\frac{\partial^2 \tilde{y}'}{\partial X^2} + \frac{\partial^2 \tilde{y}'}{\partial Z^2} \right), \tag{25}$$

$$\frac{\partial \bar{w}'}{\partial \tau} + \frac{\partial \bar{w}'}{\partial X} = \frac{\partial}{\partial Z} \left(\frac{\partial^2 \tilde{y}'}{\partial X^2} + \frac{\partial^2 \tilde{y}'}{\partial Z^2} \right), \tag{26}$$

$$\frac{\partial \bar{v}'}{\partial \tau} + \frac{\partial \bar{v}'}{\partial X} = 4 \left(\frac{\partial^2 \bar{y}'}{\partial X^2} + \frac{\partial^2 \bar{y}'}{\partial Z^2} \right), \tag{27}$$

$$\frac{\partial \bar{y}'}{\partial \tau} + \frac{\partial \bar{y}'}{\partial X} = \bar{v}'. \tag{28}$$

Equations (24)–(28) show that the sinuous mode ((27) and (28)) related to variations of $\bar{v}'$ and $\bar{y}'$ is decoupled from the dilational mode ((24)–(26)) in the linear analysis.

3.1. *Linear analysis for the dilational mode*

Equations (24)–(26) are the governing equations for the linear dilational mode of liquid sheets with infinite length and can be combined into one equation as

$$\frac{\partial^2 \tilde{y}'}{\partial \tau^2} + \frac{\partial^4 \tilde{y}'}{\partial X^4} + 2\frac{\partial^4 \tilde{y}'}{\partial X^2 \partial Z^2} + \frac{\partial^4 \tilde{y}'}{\partial Z^4} = 0. \tag{29}$$

Let us assume as a solution of (29) a wave travelling in the X-direction and standing in the Z-direction:

$$\tilde{y}' = y_o \cos lZ \exp\left[\mathrm{i}(\omega\tau - kX)\right] \tag{30}$$

where k is the dimensionless wavenumber in the X-direction, l is the dimensionless wavenumber in the Z-direction, and ω is the dimensionless frequency of the wave. Now, we perform a temporal stability analysis by assuming that ω can be complex. Insert (30) into (29) and solve for ω. Then, we get the three-dimensional dispersion relationship as

$$\omega = k^2 + l^2 \tag{31}$$

which shows that ω has only a real part. Therefore, the dilational waves on three-dimensional planar liquid sheets with infinite length are neutrally stable by a linear analysis. From (31), the wave speed is computed as $V_d = k + (l^2/k)$. The dilational mode is dispersive since the wave speed V_d depends upon k and l.

3.2. *Nonlinear numerical results for the dilational mode*

For the dilational mode, $\bar{v} = 0$, $\bar{y} = 0$, and $\Delta p = 0$, and thus, equations (19)–(21) without the $\Delta\phi$ term become a set of the governing equations.

For the dilational mode of the two-dimensional (reduced to one-dimensional) unsteady case, an analytical solution for a limit cycle exists for (19)–(20) with zero values of $\bar{w}$ and $\Delta\phi$ (Mehring & Sirignano 1999). The analytical solution shows that the product of wave speed and wavelength is dependent on the amplitude of the wave. When the amplitude of the dispersive wave is small, the wave speed V_d equals $2\pi/\lambda$ which can be predicted from a linear theory, where λ is the wavelength in the streamwise direction.

For the present three-dimensional (reduced to two-dimensional) unsteady case, an analytical solution does not exist, and (19)–(21) with zero value of $\Delta\phi$ are solved numerically. The computational domain is chosen as $0 \leqslant X \leqslant X_a$ and $0 \leqslant Z \leqslant b$, where b is the width of the liquid sheet. In the X-direction, the periodic boundary condition is imposed on each of the independent variables at $X = 0$ and at $X_a = n\lambda_x$, where n is any integer and λ_x is the wavelength of the disturbance in the X-direction. In the Z-direction, as in the X-direction, the periodic boundary condition is imposed on each of the independent variables at $Z = 0$ and b. As initial conditions, we assume a sinusoidal wave travelling in the X-direction and standing in the Z-direction so that

$$\tilde{y}(X, Z, \tau = 0) = \alpha_0 + \alpha_1 \cos(kX) \cos(lZ) \tag{32}$$

where $k = 2\pi/\lambda_x$ and $l = 2\pi/\lambda_z$. The initial conditions for $\bar{u}_1$ and $\bar{w}$ are assumed to be

$$\bar{u}_1(X, Z, \tau = 0) = \alpha_2\alpha_1(\omega/k)(\cos(kX)\cos(lZ) - \psi)/\tilde{y}, \tag{33}$$

$$\bar{w}(X, Z, \tau = 0) = (\alpha_2 - 1)\alpha_1(\omega/l)(\sin(kX)\sin(lZ))/\tilde{y} \tag{34}$$

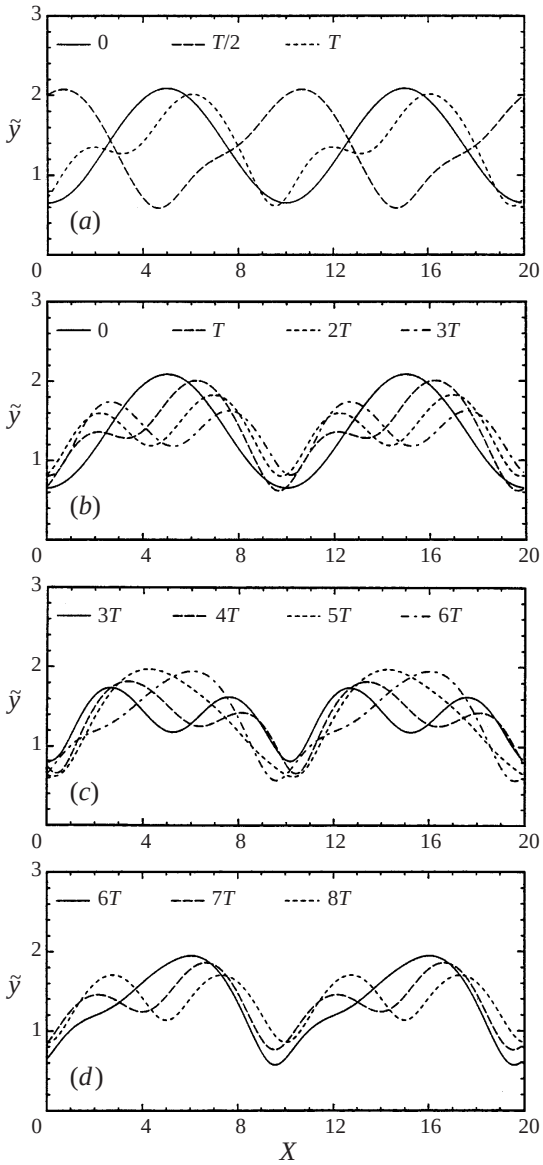

FIGURE 2. $\tilde{y}$ (sheet thickness) versus X in the plane of $Z = 0$ at: (*a*) $0 \leqslant \tau \leqslant T$; (*b*) $0 \leqslant \tau \leqslant 3T$; (*c*) $3T \leqslant \tau \leqslant 6T$; and (*d*) $6T \leqslant \tau \leqslant 8T$ with $\alpha_o = 1.37$, $\alpha_1 = -0.717$, and $\alpha_2 = 0.5$, where T is the period.

where $\omega = 2\pi/T$ and $\psi = (1 - \alpha_o)/\alpha_1$ which is obtained by assuming initially $\bar{u}_1 = 0$ at $\tilde{y} = 1$. The expressions for $\bar{u}_1$ and $\bar{w}$ are suggested by the continuity equation (19). The initial conditions of $\bar{u}_1$ and $\bar{w}$ can be arbitrary. However, arbitrary initial conditions can introduce large wave wobbling when it propagates due to a standing wave added effectively to the propagation wave in the streamwise direction (Mehring & Sirignano 1999). The initial conditions given by (32)–(34) satisfy the continuity equation (19).

Now we solve (19)–(21) with the initial conditions given by (32)–(34) and the

periodic boundary conditions mentioned earlier. $\lambda_x = 10$, $\lambda_z = 10$, $n = 2$, and $b = 20$ with $\alpha_0 = 1.37$, $\alpha_1 = -0.717$, and $\alpha_2 = 0.5$ are used in the following computations. The values of α_0 and α_1 are chosen as the first and second Fourier coefficients, respectively, of the two-dimensional (reduced to one-dimensional) analytical solution for the integration constant $C = 2.5$ by Mehring & Sirignano (1999); $\alpha_2 = 0.5$ is chosen such that the magnitudes of $\bar{u}_1$ and $\bar{w}$ are close to each other. Since the period of the wave (or frequency $\omega = 2\pi/T$) is not known in advance, a trial and error method is used to find the period. A value of T is chosen and (19)–(21) are solved with that value of T. Then, a new value of T can be found by examining the solutions as a function of time. This process continues until a correct value of T is found. $T = 6.85$ is the result.

Figure 2(*a–d*) displays $\tilde{y}$ versus X in the plane of $Z = 0$ at: (*a*) $0 \leqslant \tau \leqslant T$; (*b*) $0 \leqslant \tau \leqslant 3T$; (*c*) $3T \leqslant \tau \leqslant 6T$; and (*d*) $6T \leqslant \tau \leqslant 8T$. The initially sinusoidal disturbance propagates in the X-direction with large deformation for $0 \leqslant \tau \leqslant T$. As more time elapses, two higher-harmonic waves are generated during $T \leqslant \tau \leqslant 3T$. However, these higher-harmonic waves disappear and there is a return to the initial wave during $3T \leqslant \tau \leqslant 6T$. Results for $\tau > 6T$ indicate that this process is repeated in a cycle.

Figure 3(*a–d*) describes $\tilde{y}$ versus Z in the plane of $X = 0$ with the same parameters as in figure 2. Initially the sinusoidal disturbance oscillates standing in the Z-direction during $0 \leqslant \tau \leqslant T$. As more time elapses, the standing wave is nearly flat during $2T \leqslant \tau \leqslant 3T$, while figure 2(*b*) shows that two higher harmonic waves are generated in the X-direction during that time. However, the nearly flat wave returns to a wave with finite amplitude during $5T \leqslant \tau \leqslant 6T$, while figure 2(*c*) shows that the two higher-harmonic waves return to the initial wave in the X-direction during that time. Results for $\tau > 6T$ indicate that this process is repeated in a cycle. Of course, this cyclic exchange is inherently three-dimensional and is not captured by a two-dimensional approximation. Also, it is nonlinear and cannot be displayed by linear theory.

This periodic exchange of energy between the transverse oscillations and the streamwise oscillations does not occur when the two wavenumbers, $2\pi/\lambda_x = k$ and $2\pi/\lambda_z = l$ are disparate or the initial amplitude α_1 is small. For example, we investigated the behaviours of wave propagation for two other combinations of λ_x and λ_z with other parameters the same as before: (i) $\lambda_x = 10$, $\lambda_z = 5$, (ii) $\lambda_x = 10$, $\lambda_z = 20$. In both cases, the initially sinusoidal wave propagates in the X-direction and oscillates standing in the Z-direction with only a little deformation, and there are no higher-harmonic waves generated.

Figure 4(*a*) illustrates $\bar{u}$ versus X at $\tau = 0$ and $8T$ in the plane of $Z = 0$ with the same parameters as in figure 2. It is shown that higher harmonics in streamwise velocity $\bar{u}$ are generated in the streamwise direction when higher-harmonic waves are generated in the same direction. Figure 4(*b*) displays $\bar{w}$ versus Z at $\tau = 6T$, $6T + T/4$, $6T + T/2$, and $6T + 3T/4$ in the plane of $X = 0$. It is shown that $\bar{w}$ oscillates standing. It is found that the profile of $\bar{w}$ along Z is nearly flat during the time the standing wave is nearly flat, for example, during $2T \leqslant \tau \leqslant 3T$.

Figures 5(*a*) and 5(*b*) show three-dimensional views at $\tau = 0$ and $\tau = 3T$, respectively. Again, they illustrate that higher-harmonic waves are generated in the X-direction and the standing wave in the Z-direction becomes nearly flat.

For liquid sheets with infinite length, the total wave energy over a wavelength in each X- and Z-direction is conserved since there is no external force acting on the sheet. The wave energy consists of two types: one is the kinetic energy and the other

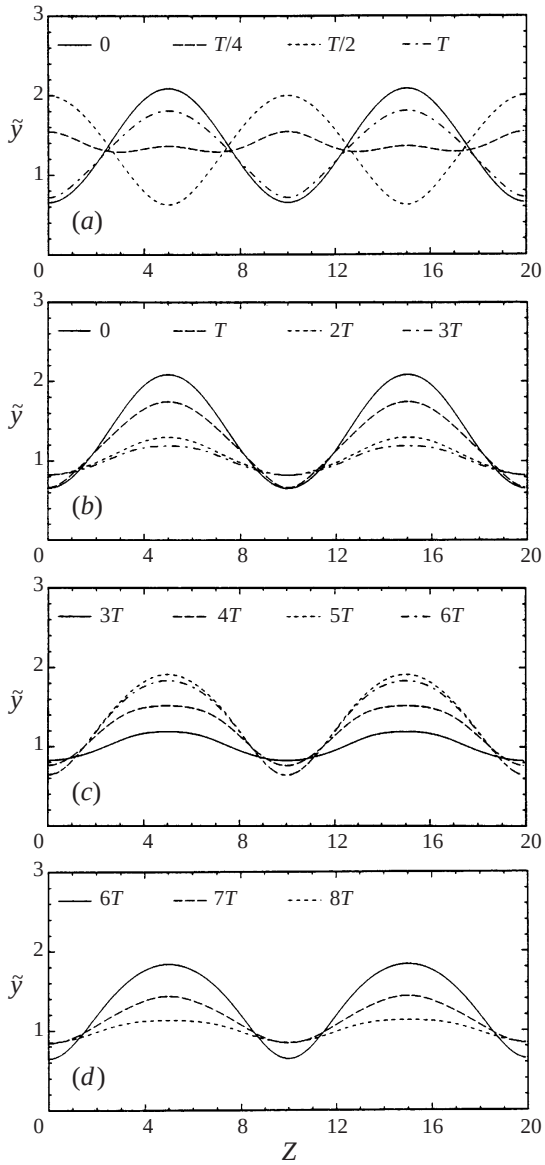

FIGURE 3. $\tilde{y}$ (sheet thickness) versus Z in the plane of $X = 0$ at: (*a*) $0 \leqslant \tau \leqslant T$; (*b*) $0 \leqslant \tau \leqslant 3T$; (*c*) $3T \leqslant \tau \leqslant 6T$; and (*d*) $6T \leqslant \tau \leqslant 8T$ with the same parameters as in figure 2, where T is the period.

is the surface energy. The kinetic energy is expressed by

$$\mathrm{KE} = \mathrm{KE}_x + \mathrm{KE}_z = \rho \int_0^{\lambda_z} \int_0^{\lambda_x} \tfrac{1}{2}(\bar{u}_1^2 + \bar{w}^2)\tilde{y}\, \mathrm{d}X\, \mathrm{d}Z$$
$$= \frac{\sigma a_o^2}{4} \int_0^{\lambda_z^*} \int_0^{\lambda_x^*} [(\bar{u}_1^*)^2 + (\bar{w}^*)^2]\tilde{y}^*\, \mathrm{d}X^*\, \mathrm{d}Z^* \tag{35}$$

where KE_x and KE_z denote the kinetic energy in the X- and Z-directions, respectively.

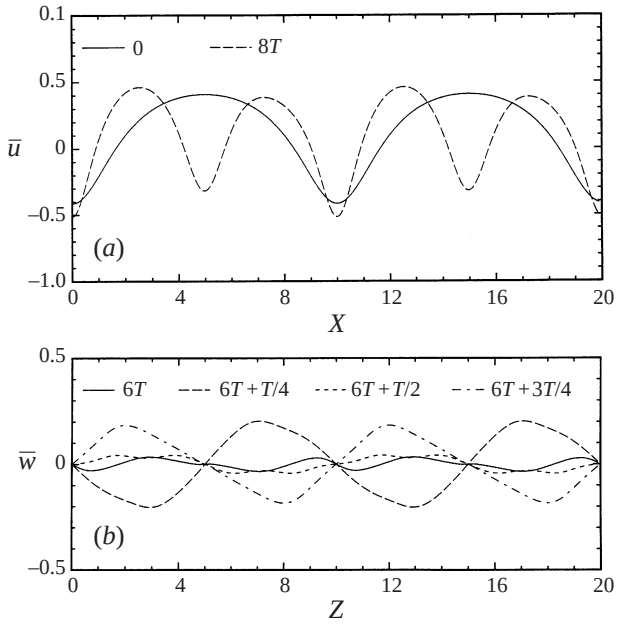

FIGURE 4. (*a*) $\bar{u}$ versus X at $\tau = 0$ and $8T$ in the plane of $Z = 0$, (*b*) $\bar{w}$ versus Z at $\tau = 6T$, $6T + T/4$, $6T + T/2$, and $6T + 3T/4$ in the plane of $X = 0$ with the same parameters as in figure 2, where T is the period.

The surface energy is related to the variation of the sheet surface area and given by

$$\begin{aligned}
\mathrm{SE} &= \mathrm{SE}_x + \mathrm{SE}_z \\
&= 2\sigma \int_0^{\lambda_z} \int_0^{\lambda_x} \sqrt{1 + \left(\frac{\partial Y_+}{\partial X}\right)^2 + \left(\frac{\partial Y_+}{\partial Z}\right)^2}\, \mathrm{d}X\, \mathrm{d}Z - 2\sigma \int_0^{\lambda_z} \int_0^{\lambda_x} \mathrm{d}X\, \mathrm{d}Z \\
&\approx 2\sigma \int_0^{\lambda_z} \int_0^{\lambda_x} \frac{1}{2} \left[\left(\frac{\partial Y_+}{\partial X}\right)^2 + \left(\frac{\partial Y_+}{\partial Z}\right)^2 \right] \mathrm{d}X\, \mathrm{d}Z \\
&= \frac{\sigma a_o^2}{4} \int_0^{\lambda_z^*} \int_0^{\lambda_x^*} \left[\left(\frac{\partial \tilde{y}^*}{\partial X^*}\right)^2 + \left(\frac{\partial \tilde{y}^*}{\partial Z^*}\right)^2 \right] \mathrm{d}X^*\, \mathrm{d}Z^*
\end{aligned} \tag{36}$$

where SE_x and SE_z denote the surface energy in the X- and Z-directions, respectively. It can be shown from (19)–(21) with $f_{1+} = f_{1-} = f_{2+} = f_{2-} = 1$ that the total wave energy over a wavelength in each direction is a time-invariant.

Next, we examine the energy of the waves computed numerically in figure 2. Figure 6 shows KE_x, KE_z, SE_x and SE_z normalized by $\sigma a_o^2/4$ as a function of time. KE_x and SE_x increase during the generation of the higher-harmonic waves in the streamwise direction; on the other hand, KE_z and SE_z decrease during the same period since the standing wave in the cross-sectional direction is flat during that time.

Figure 7 illustrates the kinetic, surface, and total energies as a function of time. The total energy is a time-invariant as mentioned above, and the kinetic and surface energies are out of phase in time with each other. Higher harmonics appear on the curves of the kinetic and surface energies as a function of time. These higher harmonics in the kinetic and surface energies as well as in the sheet thickness ($\tilde{y}$) and in the streamwise velocity ($\bar{u}$) are generated by nonlinear effects.

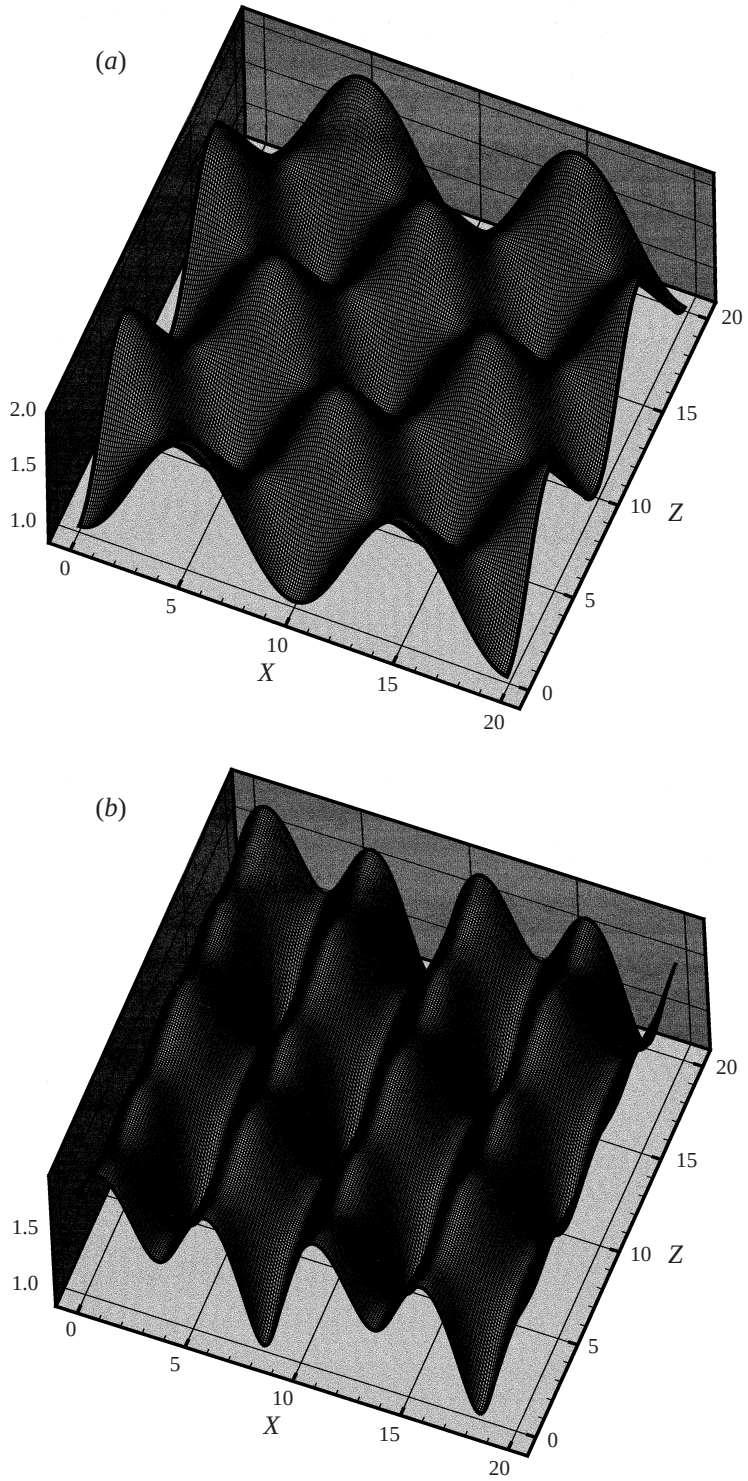

FIGURE 5. Three-dimensional views of $\tilde{y}$ at (*a*) $\tau = 0$ and (*b*) $\tau = 3T$ with the same parameters as in figure 2, where T is the period.

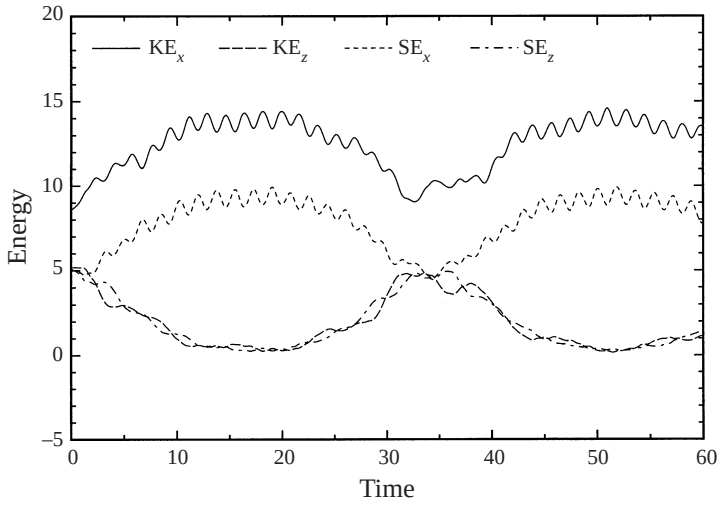

FIGURE 6. Kinetic energy in the X-direction (KE_x), kinetic energy in the Z-direction (KE_z), surface energy in the X-direction (SE_x), and surface energy in the Z-direction (SE_z) normalized by $\sigma a_o^2/4$ as a function of time.

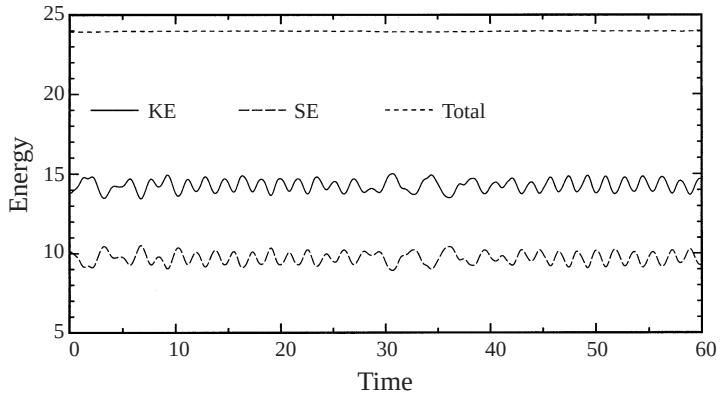

FIGURE 7. Kinetic, surface, and total energies normalized by $\sigma a_o^2/4$ as a function of time.

The numbers of grid points per wavelength in the X- and Z-directions are $N_x = 100$ and $N_z = 100$, respectively, and the time step is $\Delta\tau = 2 \times 10^{-3}$. We have checked that the accuracy of our numerical simulation does not affect the results. For instance, the maximum amplitude ($\tilde{y}$) at $\tau = 41.1$ ($6T$) is 1.94 at $X = 6.1$ and $Y = 0$. Using a doubled time step with the same number of grids results in the same amplitude 1.94 at the same time and location. Using a doubled spatial resolution in both the X- and Z-directions gives the amplitude 1.92 at the same time and location.

3.3. *Linear analysis for the sinuous mode*

Equations (27) and (28) are the governing equations for the linear sinuous mode of liquid sheets with infinite length and can be combined into one equation as

$$\frac{\partial^2 \tilde{y}'}{\partial \tau^2} + 4\frac{\partial^2 \tilde{y}'}{\partial X^2} + \frac{\partial^2 \tilde{y}'}{\partial Z^2}. \tag{37}$$

Let us assume as a solution of (37) a wave travelling in the X-direction and standing in the Z-direction:

$$\tilde{y}' = y_o \cos lZ \exp\left[\mathrm{i}(\omega\tau - kX)\right] \tag{38}$$

where k is the dimensionless wavenumber in the X-direction, l is the dimensionless wavenumber in the Z-direction, and ω is the dimensionless frequency of the wave. Now, we perform a temporal stability analysis by assuming that ω can be complex. Insert (38) into (37) and solve for ω. Then, we get the three-dimensional dispersion relationship as

$$\omega = 2\sqrt{k^2 + l^2} \tag{39}$$

which shows that ω has only a real part. Therefore, the sinuous waves on three-dimensional planar liquid sheets with infinite length are neutrally stable as are the dilational waves. From (39), the wave speed is computed as $V_s = 2\sqrt{1 + (l/k)^2}$, which indicates that the wave is dispersive when $l \neq 0$. Note that Mehring & Sirignano (1999) showed through a linear analysis that the wave speed V_s equals 2 and the wave is therefore non-dispersive for the two-dimensional sinuous mode ($l = 0$).

3.4. *Nonlinear numerical results for the sinuous mode*

For the sinuous mode, (19)–(23) are the governing equations and show that an initial transverse velocity $\bar{v}(X, Z, \tau = 0)$ induces changes not only in the sheet centreline $\bar{y}$ but also in the sheet thickness $\tilde{y}$, which means that the sinuous and dilational modes are coupled in a nonlinear analysis. Note that (24)–(28) showed that the sinuous and dilational modes are decoupled in a linear analysis.

Equations (19)–(23) are solved numerically for the present three-dimensional (reduced to two-dimensional) unsteady case. The computational domain is chosen as $0 \leqslant X \leqslant X_a$ and $0 \leqslant Z \leqslant b$, where b is the width of the liquid sheet. Similarly as in § 3.2, the periodic boundary conditions are imposed on each of the independent variables in the X- and Z-directions. For initial conditions, we assume a sinuous wave travelling in the X-direction and standing in the Z-direction. That is,

$$\bar{y}(X, Z, \tau = 0) = A \cos(kX) \cos(lZ), \tag{40}$$

$$\tilde{y}(X, Z, \tau = 0) = 1 \tag{41}$$

where $k = 2\pi/\lambda_x$, $l = 2\pi/\lambda_y$ and $\omega = 2\pi/T$. The initial condition for $\bar{v}$ is obtained from (23). Then, the initial conditions for $\bar{u}_1$, $\bar{w}$, and $\bar{v}$ are

$$\bar{u}_1(X, Z, \tau = 0) = \bar{w}(X, Z, \tau = 0) = 0, \tag{42}$$

$$\bar{v}(X, Z, \tau = 0) = A\omega \sin(kX) \cos(lZ). \tag{43}$$

Now we solve equations (19)–(23) with the initial conditions given by equations (40)–(43) and the periodic boundary conditions mentioned earlier. $\lambda_x = 50$, $\lambda_z = 50$, $X_a = 100$, and $b = 100$ are used in the following computations.

Figure 8(*a–d*) displays Y_+ (upper surface) and Y_- (lower surface) versus X in the plane of $Z = 0$ at (*a*) $\tau = 0$; (*b*) 118; (*c*) 128; and (*d*) 140 with $A = 1.375$ and $\omega = 0.32$. This figure shows that, as time passes, fluid accumulates in the edge of the sheet interspaced by half a wavelength, indicating that an initial sinuous disturbance induces not only a wave that is sinuous but also the variation of the sheet thickness (dilational mode). Figure 9(*a–d*) displays Y_+ and Y_- versus Z in the plane of $X = 0$ at the same times with the same parameters as in figure 8(*a–d*). This

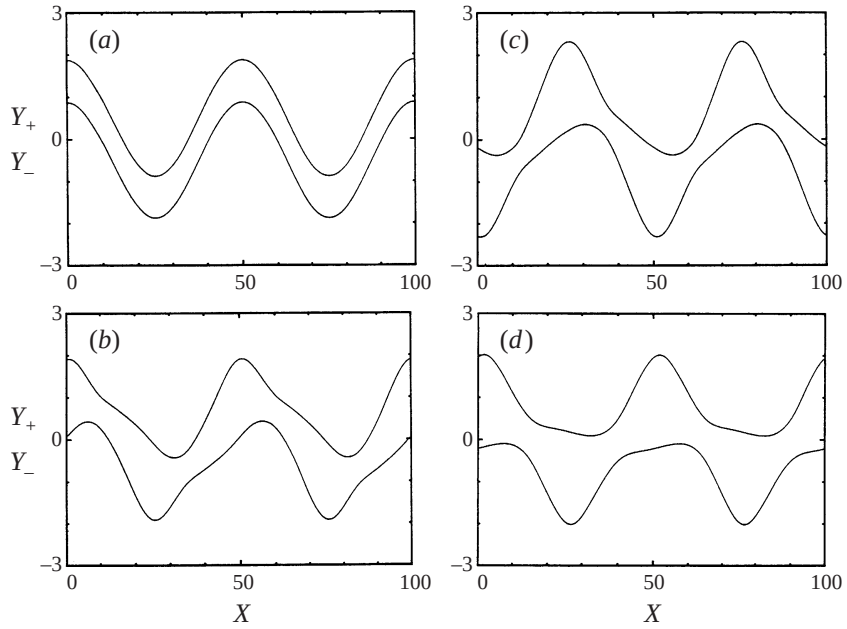

FIGURE 8. Y_+ (upper surface) and Y_- (lower surface) versus X in the plane of $Z = 0$ at (*a*) $\tau = 0$; (*b*) 118; (*c*) 128; and (*d*) 140 with $A = 1.375$ and $\omega = 0.32$.

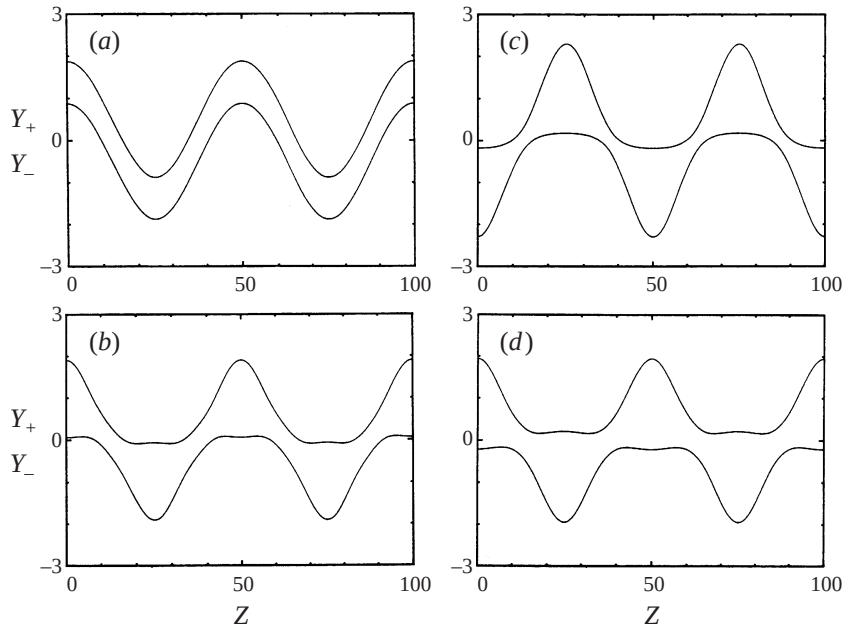

FIGURE 9. Y_+ (upper surface) and Y_- (lower surface) versus Z in the plane of $X = 0$ at (*a*) $\tau = 0$; (*b*) 118; (*c*) 128; and (*d*) 140 with the same parameters as in figure 8.

figure shows that as time passes, fluid accumulates in the cross-sectional direction as well as in the streamwise direction. As a whole, an initial sinuous disturbance with the cross-sectional wavenumber (l) close to the streamwise wavenumber (k) has fluid agglomerated in a half-spherical shape, indicating the formation of large spherical

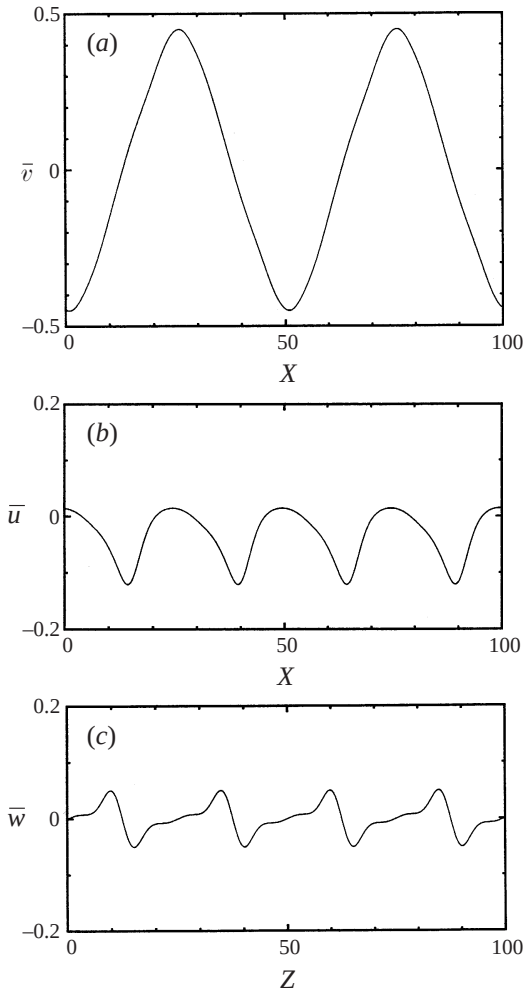

FIGURE 10. Velocity profiles: (*a*) $\bar{v}$ versus X in the plane of $Z = 0$; (*b*) $\bar{u}$ versus X in the plane of $Z = 0$; and (*c*) $\bar{w}$ versus Z in the plane of $X = 0$ at $t = 140$ with the same parameters as in figure 8.

droplets from the liquid sheet. This phenomenon will be seen more clearly in the case of modulated semi-infinitely long thin liquid sheets with sinuous disturbances (§ 4.4).

Figure 10(*a–c*) illustrates velocity profiles (*a*) $\bar{v}$ versus X in the plane of $Z = 0$; (*b*) $\bar{u}$ versus X in the plane of $Z = 0$; and (*c*) $\bar{w}$ versus Z in the plane of $X = 0$ at $t = 140$ with the same parameters as in figures 8 and 9. It shows that $\bar{v}$ oscillates in sinuous motion in the streamwise direction; $\bar{u}$ and $\bar{w}$ are initially zero, but non-zero $\bar{u}$ and $\bar{w}$ appear as time passes. As a result, the dilational mode is generated.

As mentioned in § 3.2, for liquid sheets with infinite length, the total wave energy over a wavelength in each X- and Z-direction is conserved since there is no external force acting on the sheet. The kinetic energy is expressed by

$$\mathrm{KE} = \frac{\sigma a_o^2}{4} \int_0^{\lambda_z^*} \int_0^{\lambda_x^*} [(\bar{u}_1^*)^2 + (\bar{v}^*)^2 + (\bar{w}^*)^2] \tilde{y}^* \, \mathrm{d}X^* \, \mathrm{d}Z^*. \tag{44}$$

The surface energy is related to the variation of the sheet surface area and given by

$$\mathrm{SE} = \frac{\sigma a_o^2}{2} \int_0^{\lambda_z^*} \int_0^{\lambda_x^*} \left[\left(\frac{\partial Y_+^*}{\partial X^*} \right)^2 + \left(\frac{\partial Y_-^*}{\partial X^*} \right)^2 + \left(\frac{\partial Y_+^*}{\partial Z^*} \right)^2 + \left(\frac{\partial Y_-^*}{\partial Z^*} \right)^2 \right] \mathrm{d}X^* \, \mathrm{d}Z^*. \quad (45)$$

It can be shown from (19)–(23) with $f_{1+} = f_{1-} = f_{2+} = f_{2-} = 1$ that the total wave energy over a wavelength in each direction is a time-invariant. Since no higher-harmonic waves are generated in this case (figure 8), the surface energy exchange in the X- and Z-directions as in § 3.2 is not observed.

The numbers of grid points per wavelength in the X- and Z-directions are $N_x = 150$ and $N_z = 150$, respectively, and the time step is $\Delta\tau = 2 \times 10^{-3}$. We have checked that the accuracy of our numerical simulation does not affect the results. For instance, when the same parameters are used as in figure 8, the maximum thickness amplitude ($\tilde{y}$) at $\tau = 140$ is 2.21 at $X = 1$ and $Z = 0$. Using a doubled time step with the same number of grids results in the same amplitude 2.21 at the same time and location. Using a doubled spatial resolution in both the X- and Z-directions gives the amplitude 2.19 at the same time and location.

4. Modulated semi-infinitely long liquid sheet

Consider a liquid sheet injected from $x = 0$ (jet exit) into the positive x-direction surrounded by a gas of negligible density. This case is more practical than the case of the liquid sheet with infinite length. The physical domain in x can be assumed as semi-infinite. Note that the Galilean transformation should not be used in this case because $x = 0$ should be a boundary surface of the domain. Normalize all the variables of (13)–(17) using a_o as the characteristic length and the undisturbed velocity u_o as the characteristic velocity. Equations (13)–(17) are transformed to

$$\frac{\partial \tilde{y}^+}{\partial t^+} + \frac{\partial \tilde{y}^+ \bar{u}^+}{\partial x^+} + \frac{\partial \tilde{y}^+ \bar{w}^+}{\partial z^+} = 0, \quad (46)$$

$$\frac{\partial \bar{u}_1^+}{\partial t^+} + \bar{u}^+ \frac{\partial \bar{u}^+}{\partial x^+} + \bar{w}^+ \frac{\partial \bar{u}^+}{\partial z^+} = -\frac{1}{2We} \left(\frac{\partial \bar{\phi}^+}{\partial x^+} - \frac{\Delta\phi^+}{\tilde{y}^+} \frac{\partial \bar{y}^+}{\partial x^+} \right), \quad (47)$$

$$\frac{\partial \bar{w}^+}{\partial t^+} + \bar{u}^+ \frac{\partial \bar{w}^+}{\partial x^+} + \bar{w}^+ \frac{\partial \bar{w}^+}{\partial z^+} = -\frac{1}{2We} \left(\frac{\partial \bar{\phi}^+}{\partial z^+} - \frac{\Delta\phi^+}{\tilde{y}^+} \frac{\partial \bar{y}^+}{\partial z^+} \right), \quad (48)$$

$$\frac{\partial \bar{v}^+}{\partial t^+} + \bar{u}^+ \frac{\partial \bar{v}^+}{\partial x^+} + \bar{w}^+ \frac{\partial \bar{v}^+}{\partial z^+} = -\frac{1}{2We} \frac{\Delta\phi^+}{\tilde{y}^+}, \quad (49)$$

$$\bar{v}^+ = \frac{\partial \bar{y}^+}{\partial t^+} + \bar{u}^+ \frac{\partial \bar{y}^+}{\partial x^+} + \bar{w}^+ \frac{\partial \bar{y}^+}{\partial z^+}, \quad (50)$$

where $+$ denotes the dimensionless quantity and will be dropped in the rest of the paper, and We is Weber number defined by $We = (\rho u_o^2 a_o)/\sigma$. We also define ϵ for convenience as

$$\epsilon = \frac{1}{\sqrt{2We}}. \quad (51)$$

In order to obtain basic information such as a dispersion relationship and the appropriate setting of boundary conditions, we perform a linear analysis before a nonlinear numerical analysis. Let $\tilde{y} = 1 + \tilde{y}'$, $\bar{y} = \bar{y}'$, $\bar{u} = 1 + \bar{u}'$, $\bar{v} = \bar{v}'$, and $\bar{w} = \bar{w}'$.

Insert these into (46)–(50) and assume that the primed quantities are small. After neglecting the higher-order terms, we get

$$\frac{\partial \tilde{y}'}{\partial t} + \frac{\partial}{\partial x}(\tilde{y}' + \bar{u}') + \frac{\partial \bar{w}'}{\partial z} = 0, \tag{52}$$

$$\frac{\partial \bar{u}'}{\partial t} + \frac{\partial \bar{u}'}{\partial x} = \epsilon^2 \frac{\partial}{\partial x}\left(\frac{\partial^2 \tilde{y}'}{\partial x^2} + \frac{\partial^2 \tilde{y}'}{\partial z^2}\right), \tag{53}$$

$$\frac{\partial \bar{w}'}{\partial t} + \frac{\partial \bar{w}'}{\partial x} = \epsilon^2 \frac{\partial}{\partial z}\left(\frac{\partial^2 \tilde{y}'}{\partial x^2} + \frac{\partial^2 \tilde{y}'}{\partial z^2}\right), \tag{54}$$

$$\frac{\partial \bar{v}'}{\partial t} + \frac{\partial \bar{v}'}{\partial x} = 4\epsilon^2 \left(\frac{\partial^2 \bar{y}'}{\partial x^2} + \frac{\partial^2 \bar{y}'}{\partial z^2}\right), \tag{55}$$

$$\frac{\partial \bar{y}'}{\partial t} + \frac{\partial \bar{y}'}{\partial x} = \bar{v}'. \tag{56}$$

Equations (52)–(56) show that the sinuous mode ((55) and (56)) related to variations of $\bar{v}'$ and $\bar{y}'$ is decoupled from the dilational mode ((52)–(54)) in the linear analysis.

4.1. *Linear analysis for the dilational mode*

Equations (52)–(54) are the governing equations for the linear dilational mode of liquid sheets with semi-infinite length. Let us assume as a solution of (52)–(54) a wave travelling in the x-direction and standing in the z-direction:

$$\tilde{y}' = y_o \cos lz \exp[\mathrm{i}(\omega t - kx)], \tag{57a}$$

$$\tilde{u}' = u_o \cos lz \exp[\mathrm{i}(\omega t - kx)], \tag{57b}$$

$$\tilde{w}' = w_o \sin lz \exp[\mathrm{i}(\omega t - kx)], \tag{57c}$$

where ω is the non-dimensional forcing frequency at the nozzle exit, k is the non-dimensional wavenumber in the x-direction, and l is the non-dimensional wavenumber in the z-direction. Insert the above expressions for $\tilde{y}'$, $\tilde{u}'$, and $\tilde{w}'$ into (52)–(54). Then, we get the three-dimensional dispersion relationship as

$$-\omega^2 + 2\omega k - k^2 + \epsilon^2(k^4 + 2k^2l^2 + l^4) = 0 \tag{58a}$$

or equivalently

$$\omega = k \pm \epsilon(k^2 + l^2). \tag{58b}$$

The non-dimensional phase velocity of the wave is obtained from (58b) as $V_d = \omega/k = 1 \pm \epsilon(k^2 + l^2)/k$ and can be also expressed as

$$V_d \approx 1 \quad \text{for } We \gg 2\omega^2 \quad \text{if } l \leqslant O(k). \tag{59}$$

Since velocities are normalized by the unperturbed sheet velocity u_o, the non-dimensional x-wavenumber k approximates the non-dimensional forcing frequency ω for the same condition as given in (59). In other words, the dimensional x-wavenumber $k = 2\pi/\lambda_x$ can be obtained from the relationship $V_d = \omega/k \approx u_o$ in dimensional form, where u_o and ω are known.

Since ω is prescribed as a forcing frequency at the nozzle exit, we solve (58a) for

the x-wavenumber k and get

$$k_{1,2} = \frac{1}{2\epsilon}(1 \pm \sqrt{1 - 4\epsilon^2 l^2 - 4\epsilon\omega}), \tag{60a}$$

$$k_{3,4} = \frac{1}{2\epsilon}(-1 \pm \sqrt{1 - 4\epsilon^2 l^2 + 4\epsilon\omega}). \tag{60b}$$

Bogy (1978) in his round liquid jet studies and Mehring & Sirignano (1999) for two-dimensional planar thin liquid sheets indicate that a wavenumber whose group velocity is negative should be discarded because it travels upstream from the location of disturbance at the nozzle exit. Also, negative group velocity means that the energy travels upstream from positive infinity which is not possible in the present problem. Therefore, we derive the group velocities ($C_g(k) = \mathrm{d}\omega/\mathrm{d}k$) of k_1, k_2, k_3, and k_4 and get

$$C_g(k_2, k_3) = \sqrt{1 - 4\epsilon^2 l^2 \mp 4\epsilon\omega}, \tag{61}$$

$$C_g(k_1, k_4) = -\sqrt{1 - 4\epsilon^2 l^2 \mp 4\epsilon\omega}. \tag{62}$$

The group velocities of k_1 and k_4 are negative. Therefore, the k_1 and k_4 solutions are discarded. Then, admissible solutions are k_2 and k_3. Equation (57a) shows that the wave related to k_2 is always stable because k_2 never has a positive imaginary part. The wave related to k_3 grows exponentially in the x-direction when $l > \sqrt{1 + 4\epsilon\omega}/(2\epsilon)$. However, in that case, it can be shown that the group velocity, defined as $C_g(k) = \mathrm{d}\omega/\mathrm{d}k_R$, is $-\infty$ which is not acceptable. The subscript R denotes the real part of a complex number. Therefore, the dilational mode of a three-dimensional semi-infinite sheet is stable by a linear analysis.

Note that under the same condition as given in (59), the group velocities of k_2 and k_3 are also nearly unity:

$$C_g(k_2, k_3) \approx 1 \quad \text{for } We \gg 2\omega^2 \quad \text{if } l \leqslant O(k). \tag{63}$$

Since velocities are normalized by the unperturbed sheet velocity u_o, (63) indicates that disturbance waves generated at the nozzle exit travel on the liquid sheet with a speed similar to u_o.

Now, we seek the general solution to (52)–(54) by superposing linearly the two admissible solutions when the group velocities for k_2 and k_3 are positive:

$$\tilde{y}' = \sum_{j=2}^{3} y_j \cos lz \exp\left[\mathrm{i}(\omega t - k_j x)\right].$$

Also, $\bar{u}'$ and $\bar{w}'$ are assumed in a similar fashion by following the forms of (57b) and (57c). By applying the boundary conditions for $\tilde{y}'$, $\bar{u}'$, and $\bar{w}'$ at the nozzle exit ($x = 0$) as $\tilde{y}'(x = 0, z, t) = 0$; $\bar{u}'(x = 0, z, t) = U(\cos lz)\exp(\mathrm{i}\omega t)$; $\bar{w}'(x = 0, z, t) = W(\sin lz)\exp(\mathrm{i}\omega t)$, we get

$$\tilde{y}'(x, z, t) = \frac{k_2^2 + l^2}{(k_3 - k_2)(k_2\omega + l^2)}(Uk_3 + \mathrm{i}Wl)\cos lz\left\{\exp\left[\mathrm{i}(\omega t - k_2 x)\right] - \exp\left[\mathrm{i}(\omega t - k_3 x)\right]\right\} \tag{64}$$

where U and W are complex numbers and the normalized amplitudes of $\bar{u}'$ and $\bar{w}'$, respectively, and k_2 and k_3 are given by (60a) and (60b), respectively. The amplitude of $\tilde{y}'$ is large when k_2 and k_3 are close to each other, and it is proportional to U and W.

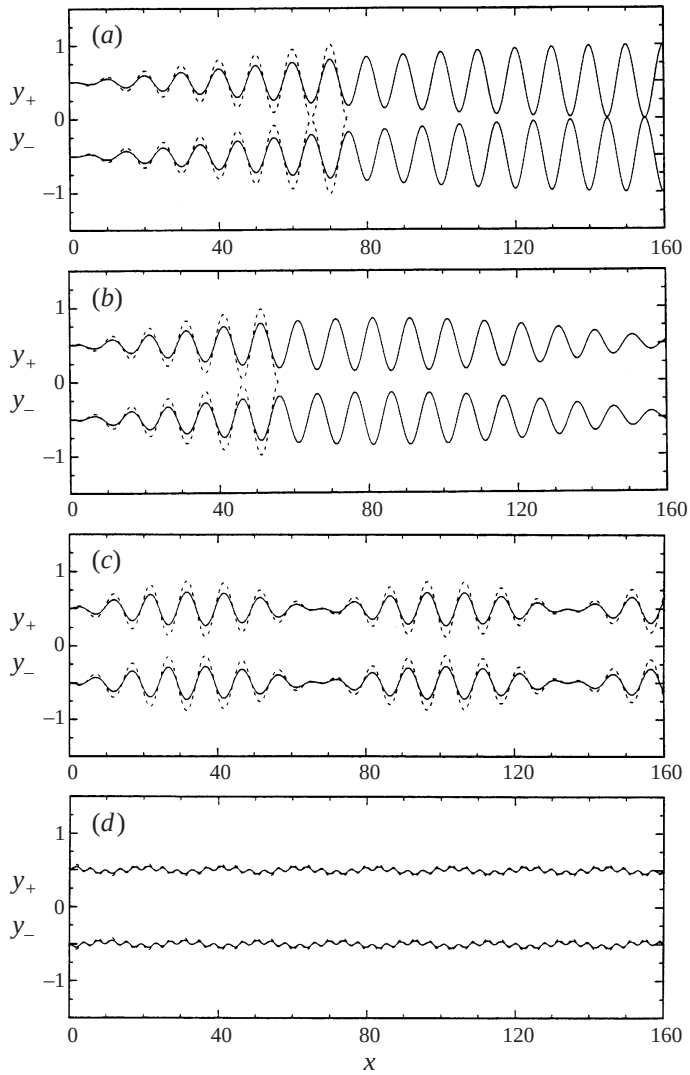

FIGURE 11. y_+ (upper surface) and y_- (lower surface) versus x in the $z = 0$ plane from the linear analysis for four cross-sectional wavenumbers (*a*) $l = 0$, (*b*) $l = \pi/5$, (*c*) $l = 2\pi/5$, (*d*) $l = 2\pi$ with $We = 900$, $\omega = \pi/5$, $U = W = -0.015\mathrm{i}$ (solid line) and $U = W = -0.025\mathrm{i}$ (dashed line), where $\mathrm{i} = \sqrt{-1}$.

Equations (60*a*) and (60*b*) indicate that k_2 and k_3 are close to each other when $\epsilon\omega$ and $\epsilon^2 l^2$ are small. Then, the two waves related to k_2 and k_3 combine and form a wave with a long-wavelength $(4\pi/(k_2 - k_3))$ envelope of a short-wavelength $(4\pi/(k_2 + k_3))$ phase, and (64) shows that the maximum amplitude of the combined wave is large. For the two-dimensional analysis ($l = 0$), Mehring & Sirignano (1999) illustrated the behaviour of $\tilde{y}'$ with variation of the forcing frequency ω. Thus, we focus on the behaviour of $\tilde{y}'$ with variation of the cross-sectional wavenumber l in the present paper.

Figure 11(*a–d*) displays the upper surface ($y_+ = 0.5\tilde{y}$) and lower surface ($y_- = -y_+$) versus x for four cross-sectional wavenumbers (*a*) $l = 0$, (*b*) $l = \pi/5$, (*c*) $l = 2\pi/5$, (*d*) $l = 2\pi$ with $We = 900$ ($\epsilon = 0.0236$), $\omega = \pi/5$, $U = W = -0.015\mathrm{i}$ (solid line)

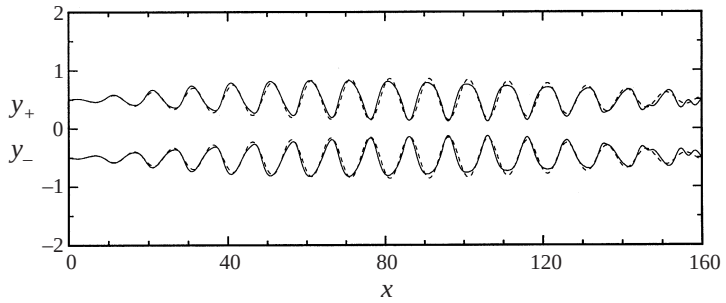

FIGURE 12. y_+ (upper surface) and y_- (lower surface) versus x in the $z = 0$ plane at $t = 180$ from the nonlinear numerical solution (solid line) and the linear analysis (dashed line) for the same parameters used in figure 11(*b*).

and $U = W = -0.025\mathrm{i}$ (dashed line), where $\mathrm{i} = \sqrt{-1}$. As l increases from zero, the maximum amplitude of the wave becomes smaller and the length of envelope becomes shorter. With $U = W = -0.015\mathrm{i}$, the liquid sheet pinches off at $x = 155$ for $l = 0$, but no zero sheet thickness occurs at this amplitude for $l > 0$. With higher amplitude $U = W = -0.025\mathrm{i}$, pinch-off of the sheet occurs for both $l = 0$ and $l = \pi/5$ but at a shorter distance from the nozzle for $l = \pi/5$ ($x = 55$) than for $l = 0$ ($x = 75$). This occurs because even if the maximum amplitude of the wave is larger for $l = 0$ than for $l = \pi/5$, it is sustained for a longer x-distance for $l = 0$ than $l = \pi/5$ due to the longer envelope for $l = 0$ than for $l = \pi/5$. It will be shown in the next subsection that nonlinear effects are greater for finite l than for $l = 0$ due to the interactions between the velocity components and pressure gradients in the x- and z-directions.

4.2. *Nonlinear numerical results for the dilational mode*

For liquid sheets with semi-infinite length, the differential equations (46)–(48) have been solved with the boundary conditions given by equations (65), (66) and (67). The liquid sheet is assumed to be initially undisturbed:

$$\tilde{y}(x = 0, z, t) = 1, \tag{65}$$

$$\bar{u}(x = 0, z, t) = 1 + U\cos(lz)\sin(\omega t), \tag{66}$$

$$\bar{w}(x = 0, z, t) = W\sin(lz)\sin(\omega t), \tag{67}$$

where U and W are the normalized amplitudes of $\bar{u}$ and $\bar{w}$, respectively. The periodic boundary condition is imposed on $\tilde{y}$, $\bar{u}$ and $\bar{w}$ at $z = 0$ and $z = \lambda_z = 2\pi/l$. The mesh size employed is $\Delta x = 0.0625$ and $\Delta z = 0.1$, and the time step is $\Delta t = 0.0125$. The boundary of the computational domain is chosen such that the propagating disturbance waves do not reach the downstream boundary within the simulation time. Accuracy of the numerical solutions has been examined by successive refinement of mesh size and time step.

First of all, we compare nonlinear numerical results with the linear analysis for a case of small amplitudes U and W. Figure 12 illustrates the upper surface (y_+) and lower surface (y_-) versus x in the $z = 0$ plane at $t = 180$ from the nonlinear numerical solution (solid line) and the linear analysis (dashed line) for the same parameters used in figure 11(*b*) ($U = W = 0.015$, $We = 900$, $\omega = \pi/5$, and $l = \pi/5$). The linear analysis predicts well the nonlinear solution for this small-amplitude case.

In the following figures, a higher amplitude is used in order to see nonlinear effects.

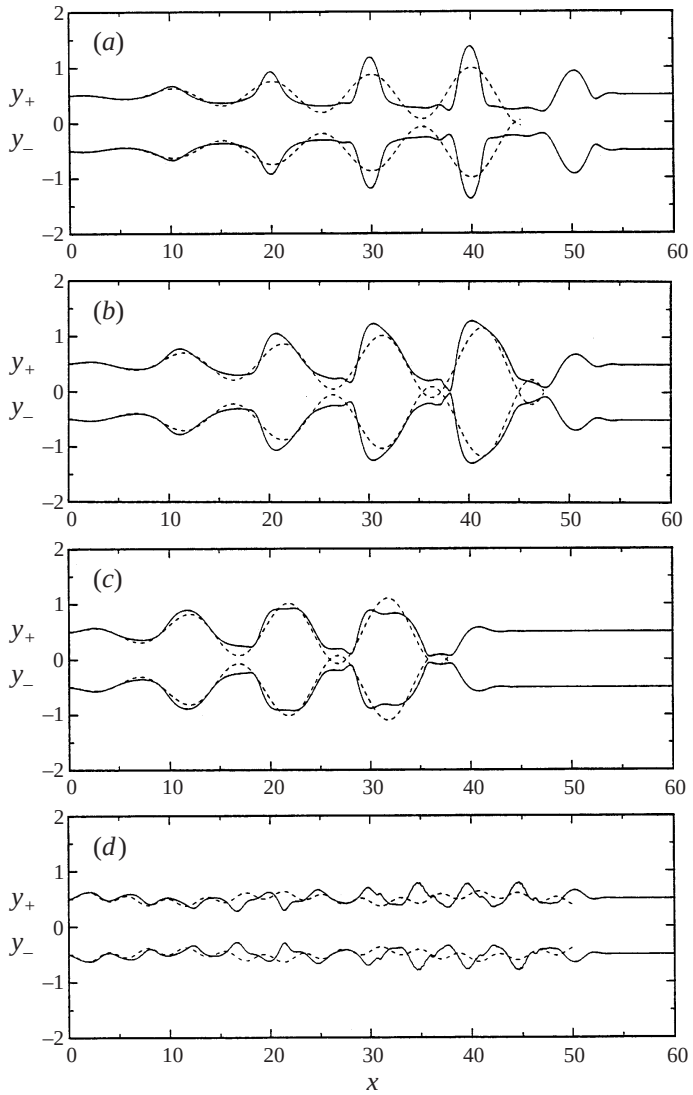

FIGURE 13. y_+ (upper surface) and y_- (lower surface) versus x in the $z = 0$ plane for four cross-sectional wavenumbers (*a*) $l = 0$, (*b*) $l = \pi/5$, (*c*) $l = 2\pi/5$, (*d*) $l = 2\pi$ at $t = 50$ except for (*c*) at $t = 40$ with $We = 900$, $\omega = \pi/5$, and $U = W = 0.04$, where the dashed lines represent solutions from the linear analysis.

Figure 13(*a–d*) displays the upper and lower sheet surfaces versus x in the $z = 0$ plane at $t = 50$ except for figure 13(*c*) at $t = 40$. Four cross-sectional wavenumbers (*a*) $l = 0$, (*b*) $l = \pi/5$, (*c*) $l = 2\pi/5$, and (*d*) $l = 2\pi$ with $We = 900$ ($\epsilon = 0.0236$), $\omega = \pi/5$, and $U = W = 0.04$ are considered, where the dashed lines represent solutions from the linear analysis. In figure 13(*a*) for $l = 0$, the nonlinear analysis illustrates that fluid accumulates into fluid lumps interspaced by one wavelength (λ_x).

Figure 13(*b*) shows that more fluid accumulates into fluid lumps for $l = \pi/5$ than for $l = 0$, and the fluid lumps are larger than those for $l = 0$ due to nonlinear interactions between the streamwise and cross-sectional directions. To understand the effect of fluid motion in the cross-sectional direction on the fluid lumps, we examined

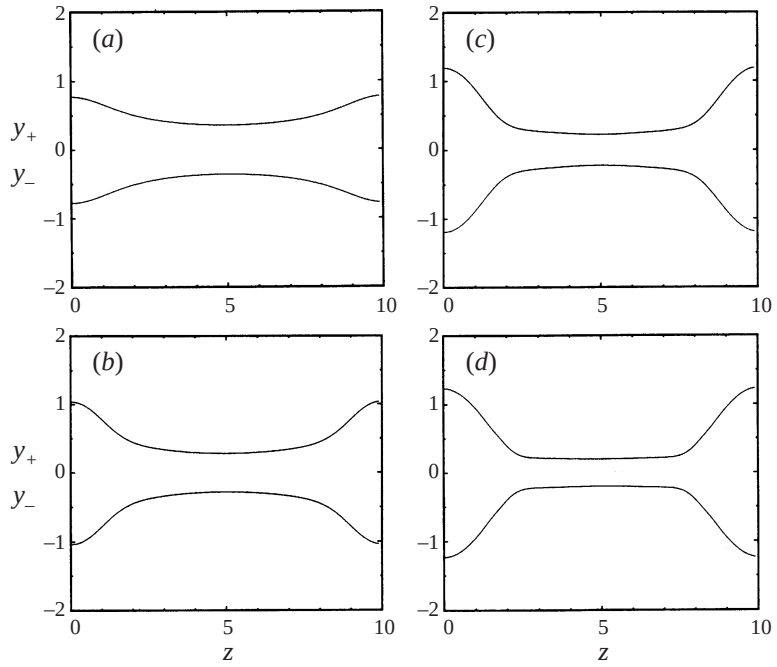

FIGURE 14. Cross-sectional view of figure 13(*b*) at four different x locations (*a*) $x = 11$, (*b*) $x = 21$, (*c*) $x = 31$, and (*d*) $x = 41$.

the cross-sectional views (figure 14*a–d*) and velocity profiles (figures 17*a* and 17*b*). Figure 17(*b*) displays the velocity component in the cross-sectional direction $\bar{w}$ versus z in the plane of $x = 41$ where the largest fluid lump occurs: $\bar{w}$ behaves such that it causes fluid to accumulate in both edges of the sheet in the z-direction as shown in the cross-sectional view of figure 14(*d*). This is the reason why the fluid lumps are larger for $l = \pi/5$ than those for $l = 0$.

As l becomes larger than $\pi/5$ (as in figures 13*c* and 13*d*), the amplitude of the wave becomes smaller, and also less fluid accumulates in the streamwise and cross-sectional directions. The streamwise wavenumber k can be obtained from the linear theory as will be explained in the following paragraph, and k is computed as $\pi/5$. As indicated in § 3, figure 13(*a–d*) shows that the strongest nonlinear effects occur when l is close to k.

Note that the wave front of the disturbance for all cases of figure 13 propagates downstream with a speed of nearly unity. The reason is that as predicted in the linear theory (§ 4.1), the group velocity of the disturbance for all these cases is nearly unity as predicted in the linear theory (equation (63)) since $We \gg 2\omega^2$. The phase velocity of the disturbance is also nearly unity when $We \gg 2\omega^2$. Therefore, the dimensionless streamwise wavenumber $k = 2\pi/\lambda_x$ can be obtained from $\omega/k = 1$.

Figure 14(*a–d*) shows the cross-sectional view of figure 13(*b*) at four different x-locations (*a*) $x = 11$, (*b*) $x = 21$, (*c*) $x = 31$, and (*d*) $x = 41$. It shows that fluid accumulates into fluid lumps interspaced by one wavelength (λ_z) in the cross-sectional direction also.

Figure 15 provides us with an overall three-dimensional view of the liquid sheet for the case of figure 13(*b*). It displays the formation of initially non-spherical ligaments or large droplets from the liquid sheet. The Weber number based upon the dimension

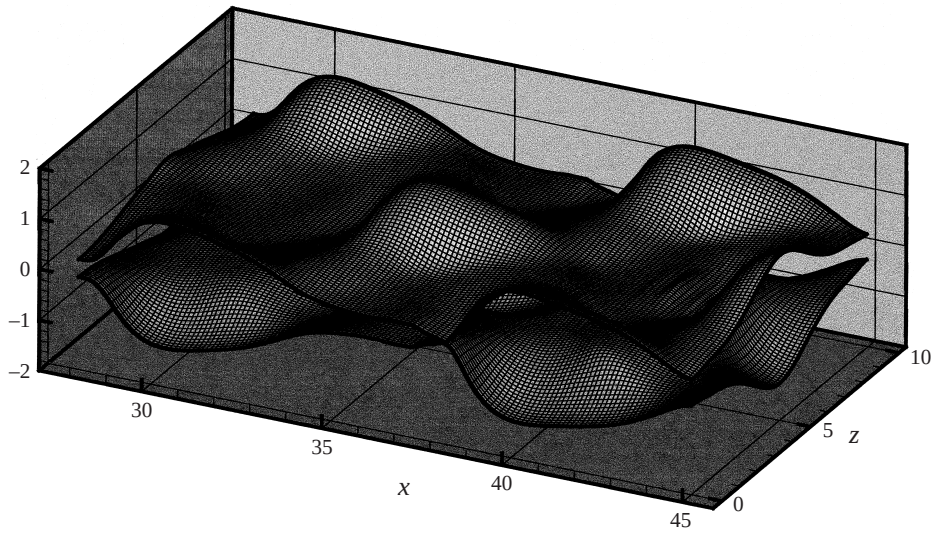

FIGURE 15. Three-dimensional view of the liquid sheet for the case of figure 13(*b*).

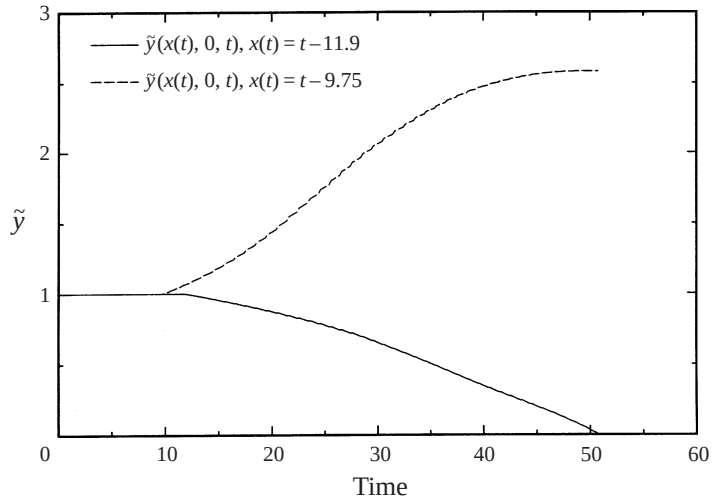

FIGURE 16. $\tilde{y}$ (sheet thickness) versus time that is obtained by following a constant phase of $\theta_1/\omega = t_1 - x_1/V_d = 50 - 38.13 = 11.9$ (solid line) and $\theta_2/\omega = t_2 - x_2/V_d = 50 - 40.25 = 9.75$ (dashed line) for the case of figure 13(*b*).

of the agglomerate will still be quite large so that further breakup into smaller droplets is conceivable.

In figures 13–15, we have illustrated the spatial dilational behaviour of the sheet surface at $t = 50$ just before the sheet is pinched off. It would be interesting to examine the time behaviour of the sheet thickness as well. The sheet thickness as a function of time in figure 16 is obtained by following a constant phase as follows. The smallest thickness occurs at $x = 38.13$ and $t = 50$ (see figure 13*b*), and the phase of this point is $\theta_1/\omega = t_1 - x_1/V_d = 50 - 38.13 = 11.9$. Thus, the sheet thickness following this phase is $\tilde{y}(x(t), z = 0, t)$, where $x(t) = t - 11.9$. The largest thickness occurs at $x = 40.25$ and $t = 50$, and the phase of this point is $\theta_2/\omega = t_2 - x_2/V_d = 50 - 40.25 = 9.75$.

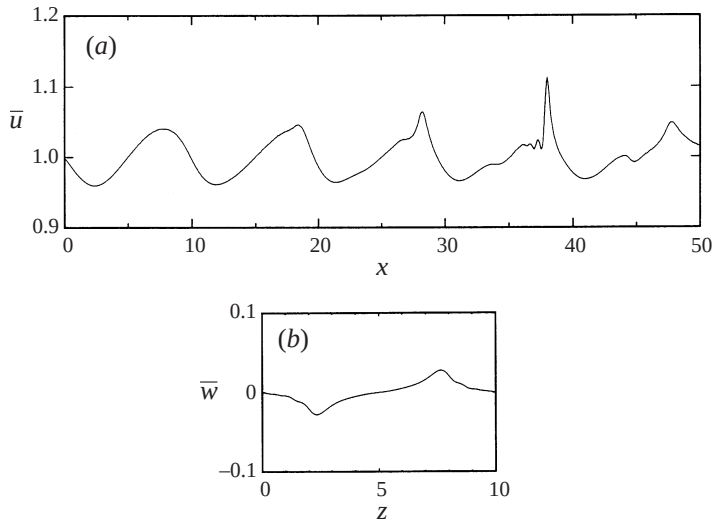

FIGURE 17. Velocity profiles: (*a*) $\bar{u}$ versus x in the plane of $z = 0$; and (*b*) $\bar{w}$ versus z in the plane of $x = 41$ at $t = 50$ with the same parameters as in figure 13(*b*).

Thus, the sheet thickness following this phase is $\tilde{y}(x(t), z = 0, t)$, where $x(t) = t - 9.75$. The solid line displays a time history of the point at which the smallest thickness occurs in the plane of $z = 0$; the dashed line displays a time history of the point at which the largest thickness occurs in the plane of $z = 0$ for the same parameters as used in figure 13(*b*). As time passes $\tilde{y}$ (solid line) at a constant phase θ_1 becomes zero algebraically from unity. On the other hand, $\tilde{y}$ (dashed line) at a constant phase θ_2 reaches its maximum about at $t = 50$, which also indicates that the amplitude of the wave envelope reaches its maximum. As explained in the previous section, for a liquid sheet dilationally modulated at the nozzle exit, the two waves are generated at the nozzle exit and form a wave with a long-wavelength envelope.

The droplet size (D_d) due to the dilational disturbance can be related to the forcing frequency (ω). For two-dimensional disturbance ($l = 0$), the volume of a ligament is $\pi r_l^2 \sim \lambda_x a_o \sim 1/\omega$. The diameter of drops produced from the ligament is $D_d = 3.78 r_l$ according to Rayleigh (1879). Therefore, $D_d \sim \omega^{-m}$, where $m = 1/2$. For a three-dimensional disturbance where $l = k$, the volume of a large droplet is $\pi D_d^3/6 \sim \lambda_x^2 a_o \sim 1/\omega^2$. Therefore, $D_d \sim \omega^{-m}$, where $m = 2/3$. Thus, the droplet size is inversely proportional to the frequency. However, the exponent m could be different from the value above when the gas density and (or) the sheet attenuation are included in the analysis.

Figures 17(*a*) and 17(*b*) display velocity profiles (*a*) $\bar{u}$ versus x in the plane of $z = 0$, and (*b*) $\bar{w}$ versus z in the plane of $x = 41$ at $t = 50$ with the same parameters as in figure 13(*b*). In the plane of $z = 0$, $\bar{u}$ oscillates in the streamwise direction, and its gradient is large at the x location where the sheet thickness is near zero. This x location would be the pinch-off position by thinning as more time passes. In the plane of $x = 41$, $\bar{w}$ behaves such that fluid accumulates in both edges of the sheet in the z-direction as shown in figure 14(*d*).

Wave propagation at low Weber number is examined in the following paragraphs. Equation (60*a*) in § 4.1 for linear analysis shows that k_2 has a negative imaginary part and thus the k_2 solution decays exponentially when $(1 - 4\epsilon^2 l^2 - 4\epsilon\omega) < 0$. Then,

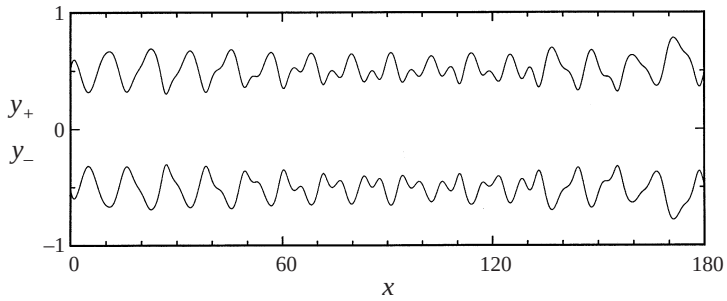

FIGURE 18. y_+ (upper surface) and y_- (lower surface) versus x in the $z = 0$ plane at $t = 32T$ for $We = 1$, $T = 6.4$, and $U = W = 0.5$ with $\lambda_z = 11.4$ ($l = 0.551$).

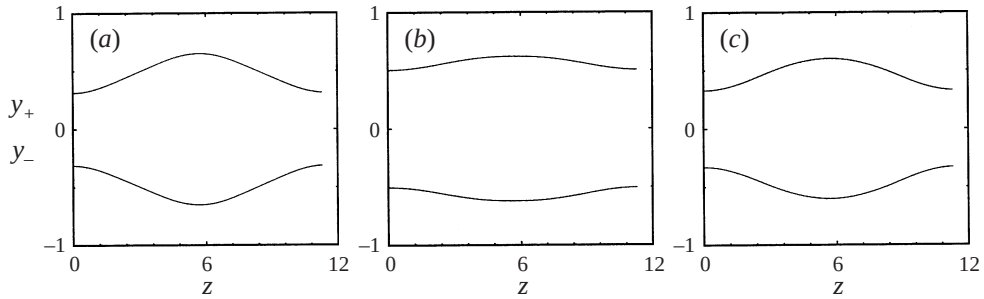

FIGURE 19. Cross-sectional views of figure 18 at three different x locations (*a*) $x = 27$, (*b*) $x = 85$, and (*c*) $x = 178$.

the beat (wave envelope) phenomenon does not occur and the k_3 solution produces sinusoidal waves on the liquid sheet as long as $(1 - 4\epsilon^2 l^2 + 4\epsilon\omega) > 0$. We have found that nonlinear solutions corresponding to this case lead to a similar phenomenon as occurs in the case of three-dimensional dilational distortion of infinite thin liquid sheets (§ 3.2). In the following figure 18, the mesh size $\Delta x = \Delta z = 0.1$ and the time step $\Delta t = 0.005$ are employed.

Figure 18 illustrates the upper and lower sheet surfaces versus x in the $z = 0$ plane at $t = 32T$ for $We = 1$ ($\epsilon = 0.707$), $T = 6.4$ ($\omega = 0.982$), and $U = W = 0.5$ with $\lambda_z = 11.4$ ($l = 0.551$). With these parameters, the linear solutions (60*a*) and (60*b*) show that k_2 has a negative imaginary part and $k_3 = 0.551$. Note that l is selected as equal to k_3. The dilational disturbance given by equations (66) and (67) with $T = 6.4$ at the nozzle exit propagates along the liquid sheet with $\lambda_x = 11.4$ ($k = 0.551$) as predicted in the linear theory up to $x \approx 40$. As it propagates downstream, two higher-harmonic waves are generated for $40 < x < 140$. However, these higher-harmonic waves disappear and there is a return to the initial wave further downstream after $x > 140$.

Figure 19(*a–c*) displays the cross-sectional views of figure 18 at three different x locations (*a*) $x = 27$, (*b*) $x = 85$, and (*c*) $x = 178$. The dilational disturbance oscillating in time and standing in the z-direction at the nozzle exit generates a standing wave in the cross-sectional (y, z)-plane of the liquid sheet as shown in figure 19(*a*) up to some distance ($0 < x < 40$) from the nozzle exit. As the wave propagates downstream, the standing wave is nearly flat as shown in figure 19(*b*), while figure 18 shows that a higher-harmonic wave component is generated at that location. As the wave propagates further downstream, the nearly flat wave returns to a standing wave with

finite amplitude as shown in figure 19(*c*), while figure 18 shows that the waveform with higher-harmonic component returns to the initial wave shape. It is noted that the amplitudes shown in figure 19(*a–c*) at three different x locations are the maximum at each location during $31T \leqslant t \leqslant 32T$. So some similarity with the temporal case is seen when λ_x and λ_z are equal. However, since continuous forced periodic oscillations in the x- and z-directions occur at the nozzle exit, we did not detect the same out-of-phase oscillations of the kinetic energies and the surface energies associated with the x- and z-directions as we did in the temporal case.

4.3. *Linear analysis for the sinuous mode*

Since the sinuous mode is decoupled from the dilational mode, (55) and (56) consist of a set of governing equations for the linear sinuous mode of liquid sheets with semi-infinite length. Let us assume as a solution of (55)–(56) a wave travelling in the x-direction and standing in the z-direction:

$$\bar{y}' = y_o \cos lz \exp[\mathrm{i}(\omega t - kx)], \tag{68a}$$

$$\bar{v}' = v_o \cos lz \exp[\mathrm{i}(\omega t - kx)], \tag{68b}$$

where ω is the non-dimensional forcing frequency at the nozzle exit, k is the non-dimensional wavenumber in the x-direction, and l is the non-dimensional wavenumber in the z-direction. Insert the above expressions for $\bar{y}'$ and $\bar{v}'$ into (55) and (56). Then, we get the three-dimensional dispersion relationship as

$$-\omega^2 + 2\omega k - (1 - 4\epsilon^2)k^2 + 4\epsilon^2 l^2 = 0 \tag{69a}$$

or equivalently

$$\omega = k \pm 2\epsilon\sqrt{k^2 + l^2}. \tag{69b}$$

The non-dimensional phase velocity of the wave is obtained from (69*b*) as $V_s = 1 \pm 2\epsilon\sqrt{1 + (l/k)^2}$ and can be also expressed as

$$V_s \approx 1 \quad \text{for } We \gg 4 \quad \text{if } l \leqslant O(k). \tag{70}$$

The three-dimensional sinuous wave is dispersive but becomes non-dispersive in the two-dimensional limit and also in the $We \to \infty$ limit. Since velocities are normalized by the unperturbed sheet velocity u_o, the non-dimensional x-wavenumber k approximates the non-dimensional forcing frequency ω for the same condition as given in (70). In other words, the dimensional x-wavenumber $k = 2\pi/\lambda_x$ can be obtained from the relationship $V_s = \omega/k \approx u_o$ in dimensional form, where u_o and ω are known.

Since ω is prescribed as a forcing frequency at the nozzle exit, we solve (69*a*) for the x-wavenumber k and get

$$k_{5,6} = \frac{1}{1 - 4\epsilon^2}[\omega \pm 2\epsilon\sqrt{\omega^2 + (1 - 4\epsilon^2)l^2}]. \tag{71}$$

As mentioned in §4.1, a wavenumber whose group velocity is negative should be discarded because it travels upstream from the location of disturbance which is the nozzle exit. Therefore, we compute the group velocities ($C_g(k) = \mathrm{d}\omega/\mathrm{d}k$) of k_5 and k_6 when they are real numbers and get

$$C_g(k_{5,6}) = 1 \mp 2\epsilon\frac{k}{\sqrt{k^2 + l^2}}. \tag{72}$$

The group velocity of k_6 is positive and thus k_6 is always acceptable when it is

a real number. On the other hand, the group velocity of k_5 is negative when $\epsilon > (1/2)\sqrt{1+(l/k_5)^2}$ (i.e. $We < 2/[1+(l/k_5)^2]$). Thus, (for large value of ϵ) k_5 is not acceptable, and only one solution (for k_6) exists under that condition.

Equation (71) shows that k_5 and k_6 become complex numbers when (i) $\epsilon > 1/2$ and (ii) $l^2 > \omega^2/(4\epsilon^2-1)$. Under these two conditions, the wave related to k_5 grows exponentially and the wave related to k_6 decays exponentially. We compute the group velocities of k_5 and k_6 when they are complex numbers and get

$$C_g(k_{5,6}) = \frac{\mathrm{d}\omega}{\mathrm{d}k_R} = 1 - 4\epsilon^2.$$

This equation shows that the group velocities of k_5 and k_6 are always negative when k_5 and k_6 are complex numbers because then $\epsilon > 1/2$. Thus, k_5 and k_6 are not acceptable due to negative group velocities when they are complex numbers. When (i) and (ii) above both apply, no linear sinuous solutions are found. When large-amplitude modulations at the nozzle exit are applied in this parameter range, the nonlinear numerical solutions yield practically undisturbed flow of the liquid away from the nozzle exit. Therefore, there are no exponentially growing or decaying waves in the sinuous mode. Thus, the sinuous mode of a three-dimensional semi-infinite sheet is neutrally stable by a linear analysis when both conditions (i) and (ii) do not apply. Note that under the same condition as given for (70), the group velocities of k_5 and k_6 are nearly unity:

$$C_g(k_{5,6}) \approx 1 \quad \text{for } We \gg 4 \quad \text{if } l \leqslant O(k). \tag{73}$$

Since velocities are normalized by the unperturbed sheet velocity u_o, (73) indicates that disturbance waves generated at the nozzle exit travel on the liquid sheet with a speed similar to u_o.

Now, we seek the general solution to (55) and (56) by superposing linearly the two admissible solutions as

$$\bar{y}' = \sum_{j=5}^{6} y_j \cos lz \exp\left[\mathrm{i}(\omega t - k_j x)\right].$$

Also, $\bar{v}'$ is assumed in a similar fashion by following the form of (68*b*). By applying the boundary conditions for $\tilde{y}'$ and $\bar{v}'$ at the nozzle exit as $\bar{y}'(x=0,z,t) = Y(\cos lz)\exp(\mathrm{i}\omega t)$ and $\bar{v}'(x=0,z,t) = V(\cos lz)\exp(\mathrm{i}\omega t)$, we get

$$\bar{y}' = \frac{\cos lz}{(k_5-k_6)}\left\{[(\omega-k_6)Y + \mathrm{i}V]\exp\left[\mathrm{i}(\omega t - k_5 x)\right] + [(k_5-\omega)Y - \mathrm{i}V]\exp\left[\mathrm{i}(\omega t - k_6 x)\right]\right\} \tag{74}$$

where Y and V are the normalized amplitudes of $\bar{y}'$ and $\bar{v}'$, respectively.

Equation (71) indicates that k_5 and k_6 are close to each other when $\epsilon\omega$ and ϵl are small compared to ω. When k_5 and k_6 are close to each other, the two waves related to k_5 and k_6 combine and form a wave with a long-wavelength $(4\pi/(k_5-k_6))$ envelope of a short-wavelength $(4\pi/(k_5+k_6))$ phase, and (74) shows that the maximum amplitude of the combined wave is large. For two-dimensional analysis ($l = 0$), Mehring & Sirignano (1999) illustrated the behaviour of $\bar{y}'$ for various forcing frequencies ω. Thus, we focus on the behaviour of $\bar{y}'$ for various cross-sectional wavenumbers l in the present paper.

Figure 20(*a–c*) displays the upper surface ($y_+ = \bar{y} + 0.5$) and lower surface ($y_- = \bar{y} - 0.5$) versus x for three cross-sectional wavenumbers (*a*) $l = 0$, (*b*) $l = \pi/5$, and (*c*) $l = 2\pi/5$ with $We = 2000$ ($\epsilon = 0.0158$), $\omega = \pi/5$, $V = 0.01$ and $Y = 0$. As l

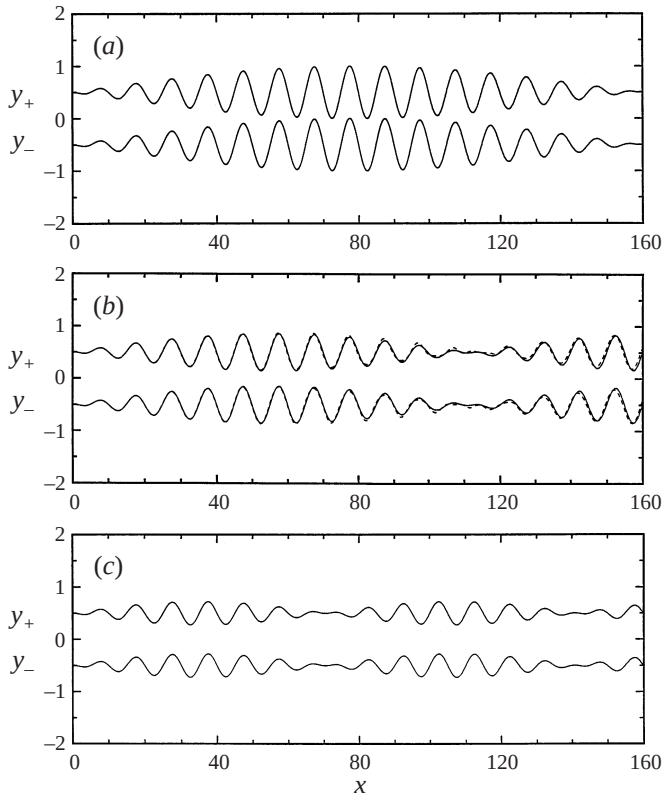

FIGURE 20. y_+ (upper surface) and y_- (lower surface) versus x from the linear analysis for three cross-sectional wavenumbers (*a*) $l = 0$, (*b*) $l = \pi/5$, and (*c*) $l = 2\pi/5$ with $We = 2000$, $\omega = \pi/5$, $V = 0.01$ and $Y = 0$, where the dashed line in (*b*) represents a solution from the nonlinear numerical solution.

becomes larger, the maximum amplitude of the wave becomes smaller and the length of envelope becomes shorter since the two wavenumbers (k_5 and k_6) of the two waves generated at the nozzle exit move apart from each other (see (71) and (74)). However, k_5 and k_6 are close enough to each other that the beat phenomenon is observed in all three cases (*a*), (*b*), and (*c*). It will be shown in the next subsection that nonlinear effects are greater for finite l than for $l = 0$ due to the interactions between the velocity components and pressure gradients in the x- and z-directions.

4.4. *Nonlinear numerical results for the sinuous mode*

For liquid sheets with semi-infinite length, the differential equations (46)–(50) have been solved with the boundary conditions

$$\tilde{y}(x = 0, z, t) = 1, \tag{75}$$

$$\bar{y}(x = 0, z, t) = Y \cos(lz) \sin(\omega t), \tag{76}$$

$$\bar{u}(x = 0, z, t) = 1, \tag{77}$$

$$\bar{v}(x = 0, z, t) = V \cos(lz) \sin(\omega t), \tag{78}$$

$$\bar{w}(x = 0, z, t) = 0, \tag{79}$$

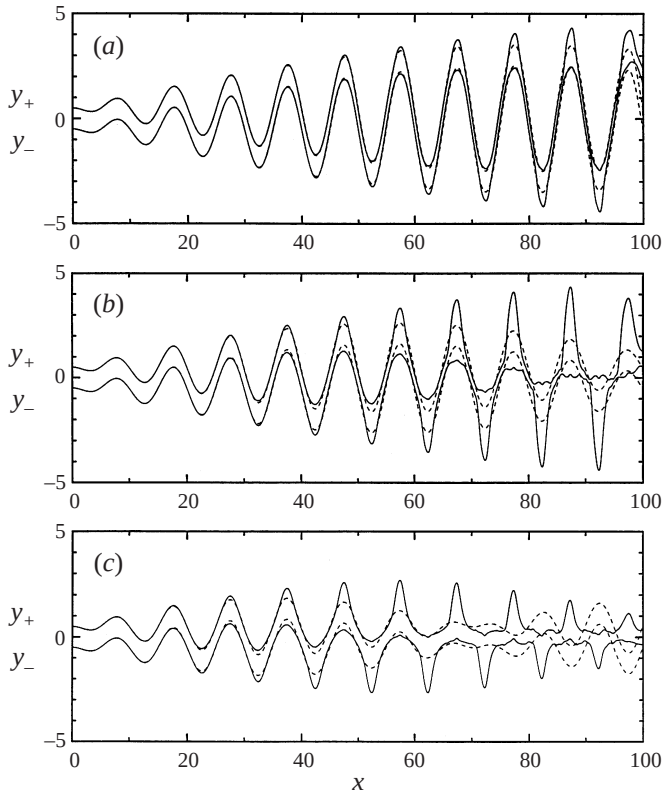

FIGURE 21. y_+ (upper surface) and y_- (lower surface) versus x at $t = 100$ for three cross-sectional wavenumbers (*a*) $l = 0$, (*b*) $l = \pi/5$, and (*c*) $l = 2\pi/5$ with $We = 2000$, $\omega = \pi/5$, $V = 0.06$, and $Y = 0$, where the dashed lines represent solutions from the linear analysis.

where Y and V are the normalized amplitudes of $\bar{y}$ and $\bar{v}$, respectively. The periodic boundary condition is imposed on $\bar{y}$, $\bar{u}$, $\bar{v}$ and $\bar{w}$ at $z = 0$ and $\lambda_z = 2\pi/l$. The liquid sheet is assumed to be initially undisturbed. The mesh size employed is $\Delta x = \Delta z = 0.05$, and the time step is $\Delta t = 0.0125$. The boundary of the computational domain is chosen such that the propagating disturbance waves do not reach the downstream boundary within the simulation time. Accuracy of the numerical solutions has been examined by successive refinement of mesh size and time step.

First of all, we compare nonlinear numerical results with the linear analysis for a case of a small amplitude V. The dashed line in figure 20(*b*) illustrates the nonlinear numerical solution at $t = 160$ for the same parameters used for the linear analysis result ($V = 0.01$, $We = 2000$, $\omega = \pi/5$, and $l = \pi/5$). The linear analysis predicts well the nonlinear solution for this small-amplitude case. In addition, the linear analysis showed in the previous section that a vertical disturbance (Y or V) induces only a wave that is sinuous. Figure 20(*b*) displays that the same is true for the nonlinear solution of the small-amplitude case.

In the following figures, a higher amplitude is used in order to see nonlinear effects. Figure 21(*a–c*) displays the upper and lower sheet surfaces versus x at $t = 100$ for three cross-sectional wavenumbers (*a*) $l = 0$, (*b*) $l = \pi/5$, and (*c*) $l = 2\pi/5$ with $We = 2000$ ($\epsilon = 0.0158$), $\omega = \pi/5$, $V = 0.06$, and $Y = 0$, where the dashed lines represent solutions from the linear analysis. In figure 21(*a*) for $l = 0$, the nonlinear

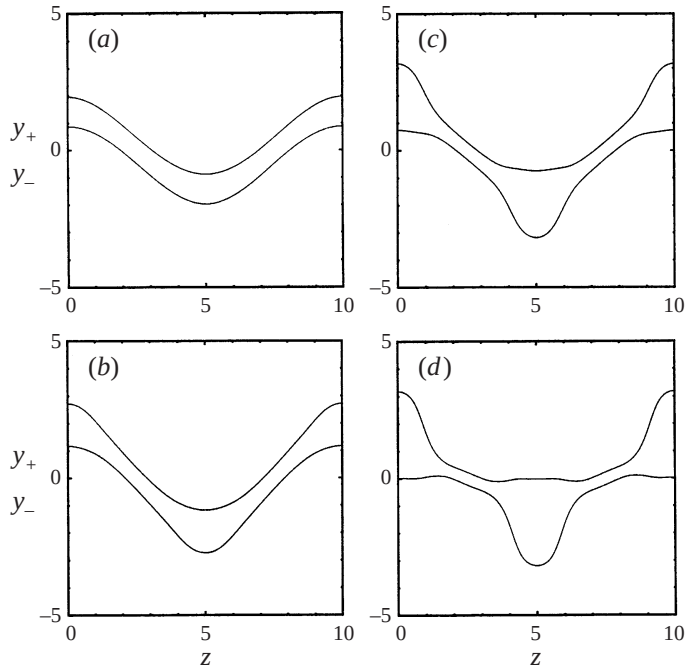

FIGURE 22. Cross-sectional view of figure 21(*b*) at four different x locations (*a*) $x = 28$, (*b*) $x = 48$, (*c*) $x = 68$, and (*d*) $x = 88$.

solution shows that fluid agglomerates in the edge of the sheet interspaced by half a wavelength ($\lambda_x/2$). This fact indicates that a vertical disturbance induces not only a wave that is sinuous but also the variation of the sheet thickness (dilational mode).

Figure 21(*b*) illustrates that more fluid agglomerates in the edge of the sheet for $l = \pi/5$ than for $l = 0$, and the sheet looks like a sawtooth. To understand the effect of fluid motion in the cross-sectional direction on the fluid agglomeration, we examined the cross-sectional views (figure 22) and velocity profiles (figure 25). Figure 25(*d*) displays the velocity component in the cross-sectional direction $\bar{w}$ versus z in the plane of $x = 88$ where the largest fluid agglomeration occurs. There is no disturbance velocity in the cross-sectional direction at the nozzle exit, i.e. $\bar{w}$ is equal to zero at the nozzle exit, but downstream at later time $\bar{w}$ is generated and behaves such that it causes fluid to accumulate near the middle and at both edges of the sheet in the z-direction as shown in the cross-sectional view of figure 22(*d*). This is the reason why the fluid agglomerations are larger for $l = \pi/5$ than those for $l = 0$.

When l is larger than $\pi/5$ (figure 21*c*), the amplitude of the wave is smaller, and also less fluid agglomerates in the streamwise and cross-sectional directions. The streamwise wavenumber k can be obtained from the linear theory as will be explained in the following paragraph, and k is computed as $\pi/5$. As indicated in § 3, figure 21(*a–c*) shows that the strongest nonlinear effects occur when l is close to k.

It should be noted that the wave front of the disturbance for all cases of figure 21 propagates downstream with a speed of nearly unity. The reason is that as predicted in the linear theory (§ 4.3), the group velocity of the disturbance for all these cases is nearly unity (equation (73)) since $We \gg 4$. The phase velocity of the disturbance is also nearly unity when $We \gg 4$. Therefore, the dimensionless streamwise wavenumber $k = 2\pi/\lambda_x$ can be obtained from $\omega/k = 1$.

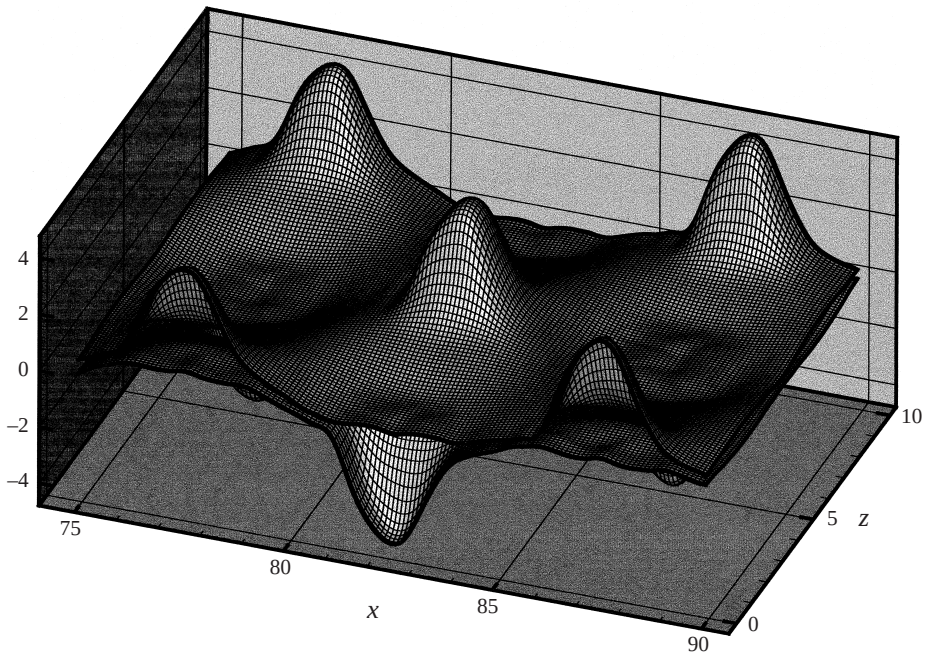

FIGURE 23. Three-dimensional view of the liquid sheet for the case of figure 21(*b*).

Figure 22(*a–d*) shows the cross-sectional view of figure 21(*b*) at four different x locations (*a*) $x = 28$, (*b*) $x = 48$, (*c*) $x = 68$, and (*d*) $x = 88$. They show that fluids agglomerate interspaced by half a wavelength ($\lambda_x/2$) in the cross-sectional direction also. Figure 23 provides us with an overall three-dimensional view of the liquid sheet for the case of figure 21(*b*). This three-dimensional view displays that the fluid agglomeration looks like a half-sphere. One can speculate that each agglomeration will eventually be distorted into a free-standing droplet. These droplets would be separated at half-wavelength intervals in both the x- and z-directions. However, the Weber number based upon the agglomerate dimension is still large so that further breakup into smaller droplets is feasible. Thin sheets connecting the half-spheres in figure 23 can be regarded as membranes which were observed experimentally by Mansour & Chigier (1990). The thin sheets are much thinner than the initial sheet, and they would contribute to the formation of smaller droplets due to viscous shear stresses.

The classical description of atomization is based on two-dimensional sinuous disturbances ($l = 0$); first, ligaments are produced separated by half-wavelengths and then these ligaments break into large droplets which would experience the second atomization later. The present paper has illustrated that the large droplets can be formed directly from the sheet when the magnitude of the disturbance at the nozzle changes sinusoidally in the cross-sectional direction. These large droplets will be produced earlier than they are with $l = 0$. Even though an experimental investigation is performed with an intention of making a two-dimensional disturbance at the nozzle exit, a three-dimensional disturbance can be introduced due to noise from the jig holding the nozzle, non-uniformity of the two-dimensional nozzle exit, or other causes. Thus, the three-dimensional pattern of figure 23 could be observed experimentally rather than two-dimensional ligaments, as shown in figures 10 and 13 of the paper by Mansour & Chigier (1990).

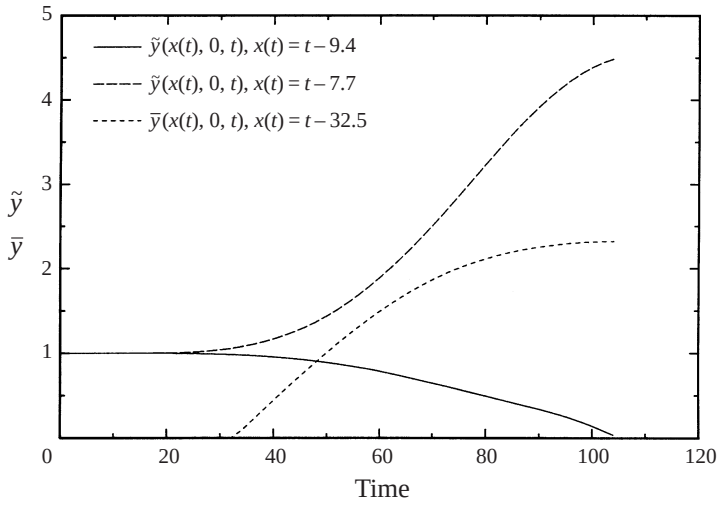

FIGURE 24. $\tilde{y}$ (sheet thickness) versus time that is obtained by following a constant phase of $\theta_1/\omega = t_1 - x_1/V_s = 104 - 94.6 = 9.4$ (solid line) and $\theta_2/\omega = t_2 - x_2/V_s = 104 - 96.3 = 7.7$ (long-dashed line); $\bar{y}$ (sheet displacement) versus time that is obtained by following a constant phase of $\theta_3/\omega = t_3 - x_3/V_s = 104 - 71.5 = 32.5$ (short-dashed line).

In figures 21–23, we have illustrated the spatial sinuous behaviour of the sheet surface at $t = 100$ just before the sheet is pinched off. We can examine the time behaviour of the sheet thickness $\tilde{y}$ and displacement $\bar{y}$ as well. The sheet thickness and displacement as a function of time in figure 24 are obtained by following a constant phase as follows. The smallest thickness occurs at $x = 94.6$ and $t = 104$ (see figure 21*b*), and the phase of this point is $\theta_1/\omega = t_1 - x_1/V_s = 104 - 94.6 = 9.4$. Thus, the sheet thickness following this phase is $\tilde{y}(x(t), z = 0, t)$, where $x(t) = t - 9.4$. The largest thickness occurs at $x = 96.3$ and $t = 104$, and the phase of this point is $\theta_2/\omega = t_2 - x_2/V_s = 104 - 96.3 = 7.7$. Thus, the sheet thickness following this phase is $\tilde{y}(x(t), z = 0, t)$, where $x(t) = t - 7.7$. The largest displacement occurs at $x = 71.5$ and $t = 104$, and the phase of this point is $\theta_3/\omega = t_3 - x_3/V_s = 104 - 71.5 = 32.5$. Thus, the sheet displacement following this phase is $\bar{y}(x(t), z = 0, t)$, where $x(t) = t - 32.5$. The solid line displays a time history of the point at which the smallest thickness occurs in the plane of $z = 0$; the long-dashed line displays a time history of the point at which the largest thickness occurs in the plane of $z = 0$; the short-dashed line displays a time history of the point at which the largest displacement of the wave occurs in the plane of $z = 0$ for the same parameters as used in figure 21(*b*). As time passes $\tilde{y}$ (solid line) of a constant phase θ_1 becomes zero algebraically from unity; $\tilde{y}$ (long-dashed line) of a constant phase θ_2 continues to increase until the sheet is pinched off. On the other hand, $\bar{y}$ (short-dashed line) of a constant phase θ_3 reaches its maximum about at $t = 104$, which also indicates that the amplitude of the wave envelope reaches its maximum. As explained in the previous section, for a liquid sheet sinusoidally modulated at the nozzle exit, the two waves are generated at the nozzle exit and form a wave with a long-wavelength envelope.

The droplet size (D_s) due to the sinuous disturbance can be related to the forcing frequency (ω). For two-dimensional disturbance ($l = 0$), the volume of a ligament is $\pi r_l^2 \sim \lambda_x a_o/2 \sim 1/\omega$. The diameter of drops produced from the ligament is $D_s = 3.78 r_l$ according to Rayleigh (1879). Therefore, $D_s \sim \omega^{-m}$, where $m = 1/2$.

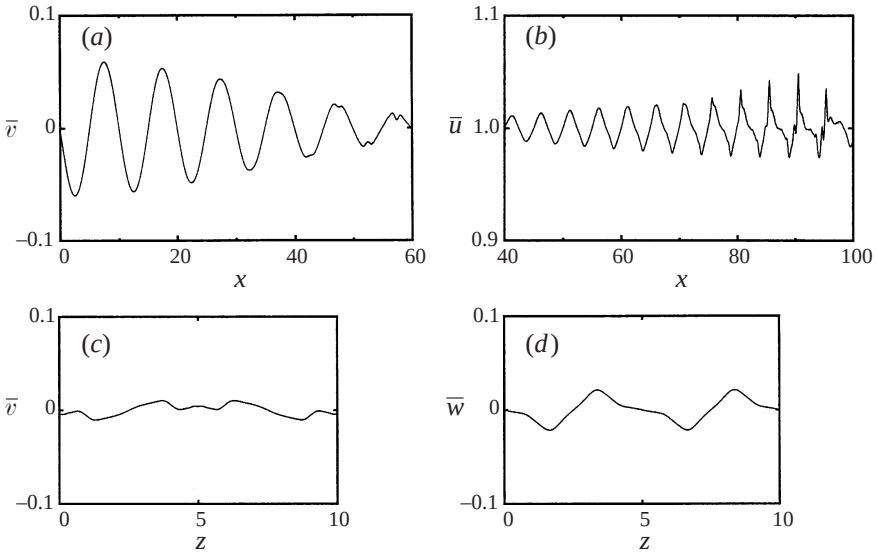

FIGURE 25. Velocity profiles (*a*) $\bar{v}$ versus x in the plane of $z = 0$; (*b*) $\bar{u}$ versus x in the plane of $z = 0$; (*c*) $\bar{v}$ versus z in the plane of $x = 88$; and (*d*) $\bar{w}$ versus z in the plane of $x = 88$ at $t = 100$ $(10T)$ with the same parameters as in figure 21(*b*).

For a three-dimensional disturbance where $l = k$, the volume of a large droplet is $\pi D_s^3/6 \sim \lambda_x^2 a_o/4 \sim 1/\omega^2$. Therefore, $D_s \sim \omega^{-m}$, where $m = 2/3$. Thus, the droplet size is inversely proportional to the frequency. However, the exponent m could be different from the value above when the gas density and (or) the sheet attenuation are included in the analysis.

Figure 25(*a–d*) displays velocity profiles (*a*) $\bar{v}$ versus x in the plane of $z = 0$; (*b*) $\bar{u}$ versus x in the plane of $z = 0$; (*c*) $\bar{v}$ versus z in the plane of $x = 88$; and (*d*) $\bar{w}$ versus z in the plane of $x = 88$ at $t = 100$ $(10T)$ with the same parameters as in figure 21(*b*). In the plane of $z = 0$ at $t = 10T$, $\bar{v}$ oscillates in the streamwise direction with its magnitude diminishing in the downstream direction; $\bar{u}$ in the plane of $z = 0$ is initially unity. As time elapses, $\bar{u}$ oscillates in the streamwise direction with its magnitude increasing in the downstream direction, and its maximum gradient becomes larger near the x location where the sheet thickness is zero. $\bar{v}$ in the plane of $x = 88$ at $t = 10T$ is nearly flat along the cross-sectional direction; $\bar{w}$ in the plane of $x = 88$ at $t = 10T$ behaves such that fluid agglomerates near the middle and at both edges of the sheet in the cross-sectional direction as shown by figure 22(*d*).

Wave propagation at low Weber number is examined in the following paragraphs. Figures 26(*a*) and 26(*b*) illustrate the upper and lower sheet surfaces versus x in the plane of $z = 0$ at $t = 120$ $(6T)$ for the cross-sectional wavenumbers $l = 0$ and $l = 0.393$, respectively, with $We = 10$ ($\epsilon = 0.2236$), $\omega = \pi/10$, $V = 0.2$, and $Y = 0$, where the dashed lines represent solutions from the linear analysis. For low Weber number cases such as figures 26(*a*) and 26(*b*), the linear analysis in § 4.3 shows that two waves are generated at the nozzle exit if $We > 2/[1 + (l/k_5)^2]$, and the group velocities of the two waves are very different from each other. The group velocities for k_5 and k_6 in figure 26(*a*) are 0.553 and 1.447, respectively, from (72). (The wavenumbers k_5 and k_6 can be obtained from (71) and are 0.568 and 0.217, respectively.) Thus, the second wave propagates much faster than the first wave. The distance over which the second wave travels is $L(k_6) = C_g(k_6)t = 174$ and can

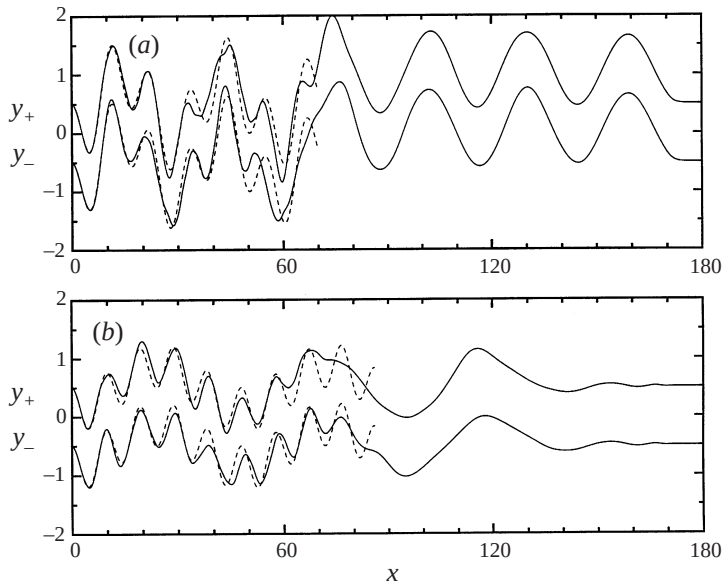

FIGURE 26. y_+ (upper surface) and y_- (lower surface) versus x in the plane of $z = 0$ at $t = 120$ $(6T)$ for the cross-sectional wavenumbers (*a*) $l = 0$ and (*b*) $l = 0.393$ with $We = 10$, $\omega = \pi/10$, $V = 0.2$, and $Y = 0$, where the dashed lines represent solutions from the linear analysis.

be identified in figure 26(*a*). On the other hand, the distance over which the first wave travels is $L(k_5) = C_g(k_5)t = 66$. As a consequence, over the first part of the sheet $0 \leqslant x \leqslant 66$, the first and second waves are combined, but over the other part $66 < x \leqslant 174$, only the second wave appears as shown in figure 26(*a*). Note that the solution from the linear analysis is a steady solution so that it shows the two waves combined over the whole length of the sheet. A similar phenomenon occurs in figure 26(*b*), where the group velocities for k_5 and k_6 are 0.86 and 1.14, respectively. (The wavenumbers k_5 and k_6 are 0.656 and 0.129, respectively.) The distance over which the second wave travels is $L(k_6) = C_g(k_6)t = 137$. On the other hand, the distance over which the first wave travels is $L(k_5) = C_g(k_5)t = 103$. As a consequence, over the first part of the sheet $0 \leqslant x \leqslant 103$, the first and second waves are combined, but over the other part $103 < x \leqslant 137$, only the second wave appears as shown in figure 26(*b*).

5. Conclusions

Three-dimensional effects on thin inviscid infinite planar liquid sheets or modulated semi-infinite planar liquid sheets in a gas of negligible density have been examined by means of a similar approach to that of Mehring & Sirignano (1999) who reduced the two-dimensional unsteady problem to a one-dimensional unsteady problem. Four different cases are considered: (i) dilational mode and (ii) sinuous mode on infinite sheets, and (iii) dilational mode and (iv) sinuous mode on modulated semi-infinite sheets. In all four cases, the strongest nonlinear effects occur when the cross-sectional wavenumber (l) is close to the streamwise wavenumber (k) for finite-amplitude disturbances.

For infinitely long sheets, the governing equations are transformed by the Galilean transformation in the streamwise direction and normalized using the undisturbed sheet

thickness a_o as the characteristic length and $\sqrt{\sigma/(2\rho a_o)}$ as the characteristic velocity. Weber number does not appear in the final dimensionless governing equations as a dimensionless parameter. Conversely, for modulated semi-infinite sheets, the Galilean transformation should not be used because the nozzle exit ($x = 0$) should be a boundary surface of the domain. The governing equations are normalized using a_o as the characteristic length and the undisturbed velocity u_o as the characteristic velocity. Weber number appears in the final dimensionless governing equations as a dimensionless parameter.

First, dilational (symmetric) wave propagations are considered. When l is close to k for infinite sheets, higher-harmonic waves are generated in the streamwise direction, and the standing wave with finite amplitude in the cross-sectional plane becomes flat. As time passes, the higher-harmonic waves return to the initial wave shape, while the flat wave returns to a standing wave with finite amplitude. This process is repeated in a cycle. This periodic exchange of kinetic energy (or surface energy) between the streamwise and cross-sectional oscillations does not occur when the two wavenumbers are disparate. A similar phenomenon is found when l is close to k for semi-infinite sheets with low Weber number.

When l is close to k for semi-infinite sheets with high Weber number, fluid accumulates into fluid lumps interspaced by one wavelength in the cross-sectional direction as well as in the streamwise direction. The fluid lumps are larger than those for $l = 0$ due to nonlinear interactions between the streamwise and cross-sectional directions. The velocity disturbance $\bar{w}$ in the cross-sectional direction oscillates sinusoidally at the nozzle exit. However, due to the nonlinearity, $\bar{w}$ behaves such that it causes fluid to accumulate in the fluid lumps in the cross-sectional direction in the downstream flow at later time. This accumulation leads to the formation of initially non-spherical ligaments or large droplets from the liquid sheet.

Secondly, sinuous (anti-symmetric) wave propagations are considered. Nonlinear numerical simulations show that at later time not only sinuous waves propagate along the sheet, but also dilational waves are generated on the sheet. When l is close to k for semi-infinite sheets with high Weber number, fluid agglomerates in the edge of the sheet interspaced by half a wavelength not only in the streamwise direction but also in the cross-sectional direction. The fluid agglomeration is larger than for $l = 0$. There is no velocity disturbance $\bar{w}$ in the cross-sectional direction at the nozzle exit. However, $\bar{w}$ is generated downstream at later time and behaves such that it causes fluid to agglomerate in fluid lumps in the cross-sectional direction. The fluid agglomeration resembles a half-sphere, which indicates the formation of ligaments or large droplets from the liquid sheet. A similar phenomenon is found in the case of three-dimensional sinuous distortion of infinite thin liquid sheets.

When Weber number is low for semi-infinite sheets, two waves are generated at the nozzle exit if $We > 2/[1 + (l/k_5)^2]$, and the group velocities (and wavenumbers) of the two waves are very different from each other. The second wave propagates much faster than the first wave. As a consequence, over the upstream part of the sheet, the first and second waves are combined, but only the second wave appears downstream.

For modulated semi-infinite sheets with high Weber number, the droplet size (D_s) can be related to the forcing frequency (ω). For a two-dimensional disturbance ($l = 0$), $D_s \sim \omega^{-m}$, where $m = 1/2$. For a three-dimensional disturbance where $l = k$, $D_s \sim \omega^{-m}$, where $m = 2/3$. Thus, the droplet size is inversely proportional to the frequency. However, the exponent m could be different from the value above when the gas density and (or) the sheet attenuation are included in the analysis.

This work is supported by the Army Research Office and monitored by Dr David Mann under the ARO Grant/Contract No. DAAH 04-96-1-0055. The support of the San Diego Supercomputer Center under a block grant of the Office of Academic Computing of UCI is gratefully appreciated.

REFERENCES

Asare, H. R., Takahashi, R. K. & Hoffman, M. A. 1981 Liquid sheet jet experiments: comparison with linear theory. *Trans. ASME*: *J. Fluids Engng* **103**, 595–604.

Bogy, D. B. 1978 Wave propagation and instability in a circular semi-infinite jet harmonically forced at the nozzle. *Trans. ASME*: *J. Appl. Mech.* **45**, 469–474.

Clark, C. J. & Dombrowski, N. 1972 Aerodynamic instability and disintegration of inviscid liquid sheets. *Proc. R. Soc. Lond.* A **329**, 467–478.

Crapper, G. D. & Dombrowski, N. 1984 A note on the effect of forced disturbances on the stability of thin liquid sheets and on the resulting drop size. *Intl J. Multiphase Flow* **10**, 731–736.

Crapper, G. D., Dombrowski, N. & Pyott, G. A. D. 1975 Large amplitude Kelvin–Helmholtz waves on thin liquid sheets. *Proc. R. Soc. Lond.* A **342**, 209–224.

Dombrowski, N. & Hooper, P. C. 1963 The effect of ambient density on drop formation in sprays. *Chem. Engng Sci.* **18**, 203–214.

Ferziger, J. H. 1981 *Numerical Methods for Engineering Application.* John Wiley & Sons.

Hagerty, W. W. & Shea, J. F. 1955 A study of the stability of plane fluid sheets. *Trans. ASME*: *J. Appl. Mech.* **22**, 509–514.

Li, X. & Tankin R. S. 1991 On the temporal instability of a two-dimensional viscous liquid sheet. *J. Fluid Mech.* **226**, 425–443.

Lin, S. P. & Roberts, G. 1981 Waves in a viscous liquid curtain. *J. Fluid Mech.* **112**, 443–458.

Mansour, A. & Chigier, N. 1990 Disintegration of liquid sheets. *Phys. Fluids* A **2**, 706–719.

Mansour, A. & Chigier, N. 1991 Dynamic behavior of liquid sheets. *Phys. Fluids* A **3**, 2971–2980.

Mehring, C. & Sirignano, W. A. 1999 Nonlinear capillary wave distortion and disintegration of thin planar liquid sheets. *J. Fluid Mech.* **388**, 69–113.

Rangel, R. H. & Sirignano, W. A. 1991 The linear and nonlinear shear instability of a fluid sheet. *Phys. Fluids* A **3**, 2392–2400.

Rayleigh, Lord 1879 On the instability of jets. *Proc. Lond. Math. Soc.* **10**, 4–13.

Squire, H. B. 1953 Investigation of the instability of a moving fluid film. *Br. J. Appl. Phys.* **4**, 167–169.

Taylor, G. I. 1959*a* The dynamics of thin sheets of fluid, II. Waves on fluid sheets. *Proc. R. Soc. Lond.* A **253**, 296–312.

Taylor, G. I. 1959*b* The dynamics of thin sheets of fluid, III. Disintegration of fluid sheets. *Proc. R. Soc. Lond.* A **253**, 313–321.